Catal Lett (2016) 146:861–885
DOI 10.1007/s10562-016-1735-4

PERSPECTIVES

Hybrid Density Functionals Applied to Complex Solid Catalysts: Successes, Limitations, and Prospects

Joachim Paier[1]

Received: 8 March 2016 / Accepted: 11 March 2016 / Published online: 26 March 2016

Abstract Density functional theory (DFT), employing semilocal approximations to describe electron exchange and correlation effects, tremendously advanced the research in the realm of computational catalysis. It allows to calculate atomic and electronic structure details of extended systems like bulk solids, surfaces or nanoparticles with reasonable accuracy at moderate computational cost. However, semilocal approximations suffer from shortcomings such as self-interaction errors (SIEs). This work discusses results obtained using two established and related approaches, namely DFT + U and orbital-dependent hybrid density functionals. Both methods partially alleviate some of the problems incurred by SIEs and are widely used in the computational community. We discuss four case studies involving reducible oxide materials: (i) the oxidative dehydrogenation of methanol at small vanadium oxide clusters supported on the $CeO_2(111)$ surface, (ii) the adsorption of Au atoms on the reduced $CeO_2(111)$ surface, (iii) stabilities of various terminations of the $V_2O_3(0001)$ surface, and (iv) the adsorption of water on the $Fe_3O_4(111)$ surface. Compared with semilocal functionals including DFT + U, we report substantial improvements in band gaps, defect formation energies, as well as activation barriers and emphasize the important role of state-of-the-art experiments for assessing DFT. Limitations of hybrid functionals due to the imposed computational workload and inherent functional approximations are discussed. To overcome these limitations, alternatives in terms of generalized RPA and embedded wavefunction-based methods are suggested.

Graphical Abstract

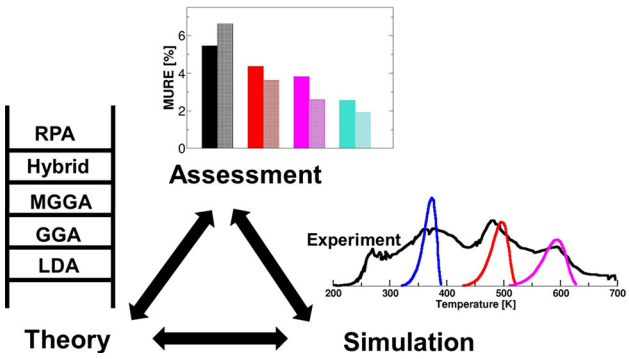

Keywords Density functional theory · Computational catalysis · Cerium oxide · Vanadium oxide · Methanol oxidation · Magnetite · Support effect · Gold adatoms · Electron transfer

1 Introduction

Density functional theory (DFT) after Kohn and Sham (KS) [1–3] based on the local density (LDA) or generalized-gradient approximation (GGA) to electron exchange and correlation (xc) is important in materials science and catalysis, because it provides atomic as well as electronic structure information of extended systems at a low computational cost. LDA was and very often is the favorite choice in the condensed matter community (e.g., [4]). The advent of GGA functionals and—few years later—the

✉ Joachim Paier
joachim.paier@chemie.hu-berlin.de

[1] Institut für Chemie, Humboldt-Universität zu Berlin, Unter den Linden 6, 10099 Berlin, Germany

introduction of orbital-dependent hybrid functionals convinced also the chemistry community to value DFT, as recently discussed by Walter Thiel [5]. With regard to molecular chemistry, LDA cannot be used, because of unacceptably large errors in binding or atomization energies [6, 7]. Conversely, errors in a number of solid-state properties obtained using LDA and GGA are comparable in magnitude. The sign of these errors may be opposite though [8].

GGA functionals provide fairly accurate molecular structures and structures of metal clusters [9, 10]. They offer sensible insights into basic material properties such as band structures and lattice parameters of simple metals, semiconductors, and insulators [11–13]. Total energy calculations employing GGA functionals are fast, and atomic forces can be evaluated at little extra computational cost. The numerical workload using GGA scales moderately with system size [14, 15], and convergence of the total energy with respect to the size of the employed basis set is easier to achieve compared to wavefunction-based methods (see, e.g., [16, 17]).

Supposed that all technical parameters employed in calculations have been converged, remaining errors are exclusively due to the approximate description of xc effects. In addition to the errors incurred by DFT (vide infra), the technical quality of selected structural models for extended systems may also affect the accuracy of results. For instance, single crystal surfaces or thin crystalline films may be modelled using clusters or slabs [18–20]. Cluster models offer the possibility to employ more accurate wavefunction-based approaches [21–23]. This allows to calculate local properties like adsorption energies with high accuracy. Slab models exploiting periodic boundary conditions may be more efficient in computing other properties like surface energies or band-structures. Finite size effects in both cluster and slab models prevent the system under study to relax or reconstruct appropriately, significantly affecting stability and reactivity.

LDA and GGA functionals suffer from so-called self-interaction errors (SIEs) [24, 25], which manifest themselves in overly delocalized orbitals and notoriously underestimated band gaps (see [26] and references therein). SIEs may drastically affect the accuracy of computational results, as discussed in many recent review articles focusing on reducible or semiconducting metal oxides [27–30]. GGAs underestimate activation barriers [31]. This is related to the fact, that a GGA functional does not correctly describe the "stretched bond" situation encountered in a transition state [32]. Related to a different type of error, GGAs fall short of correct dispersion-type van der Waals interactions [33]. The latter may substantially affect calculated adsorption energies, i.e. the stability of the adsorption complex [34]. Extensive methodologically motivated discussions on these shortcomings can be found in [35, 36] and [37].

Surfaces of reducible metal oxides are interesting model systems for oxidation reactions in catalysis [38, 39]. However, the accurate description of their physical and chemical properties by DFT represents a formidable task. The various 3d transition metal oxide phases of, e.g., vanadium, chromium, and iron as well as oxides of rare-earth metals like cerium featuring 4f orbitals represent particularly challenging systems from a computational point of view. As mentioned in [27, 29], cerium oxides (ceria) require methods that are capable to describe 4f orbitals involved in bonding as well as in the spatially localized (reduced) Ce^{III}. Oxides like Fe_2O_3, also known as Mott–Hubbard systems, have partially occupied d orbitals being subject to strong intra-atomic Coulomb correlation effects. A correct description of the latter is largely elusive to the GGA approximation [37, 40].

In catalysis, surface oxygen defects play a central role in the Mars-van Krevelen oxidation mechanism [41]. Oxygen defect formation energies are important descriptors to assess the activity of an oxide catalyst [42]. Formation of O defects in insulating reducible oxides incurs occupation of energetically low lying empty d or f orbitals, which implies formation of defect-induced electronic states below the conduction band minimum. Since GGA functionals substantially underestimate band gaps, electron occupation of the conduction band is energetically too facile. Instead of the formation of a defect state within the gap, the reduced system may spuriously metallize. The spatially localized nature of the defect state is lost, as shown for an O defect in the $CeO_2(111)$ surface (cf. Fig. 1a). Similar problems occur, if positively charged holes in the O 2p valence band are formed upon introduction of undervalent substitutional or interstitial cationic point defects (*p*-type doping) [43–45]. This shortcoming affects defect formation energies.

Hence, alleviating the band gap problem as well as overdelocalization may improve the accuracy in thermodynamic properties. However, we underline that a correct gap alone is not a sufficient condition for accurate thermodynamic predictions based on DFT [29].

Examining several case studies, this work provides evidence that hybrid functionals offer an improved description of reducible oxides for a number of properties including activation barriers as well as localization of charges and spins of electrons. With regard to defect formation energies, hybrid functionals outperform the commonly applied and less compute intensive DFT + U approach. We discuss (i) activation barriers in the oxidative dehydrogenation of methanol at small vanadium oxide clusters supported on the $CeO_2(111)$ surface, (ii) the adsorption of Au atoms on the reduced $CeO_2(111)$ surface, (iii) stabilities of various terminations of the $V_2O_3(0001)$ surface, and (iv) the adsorption

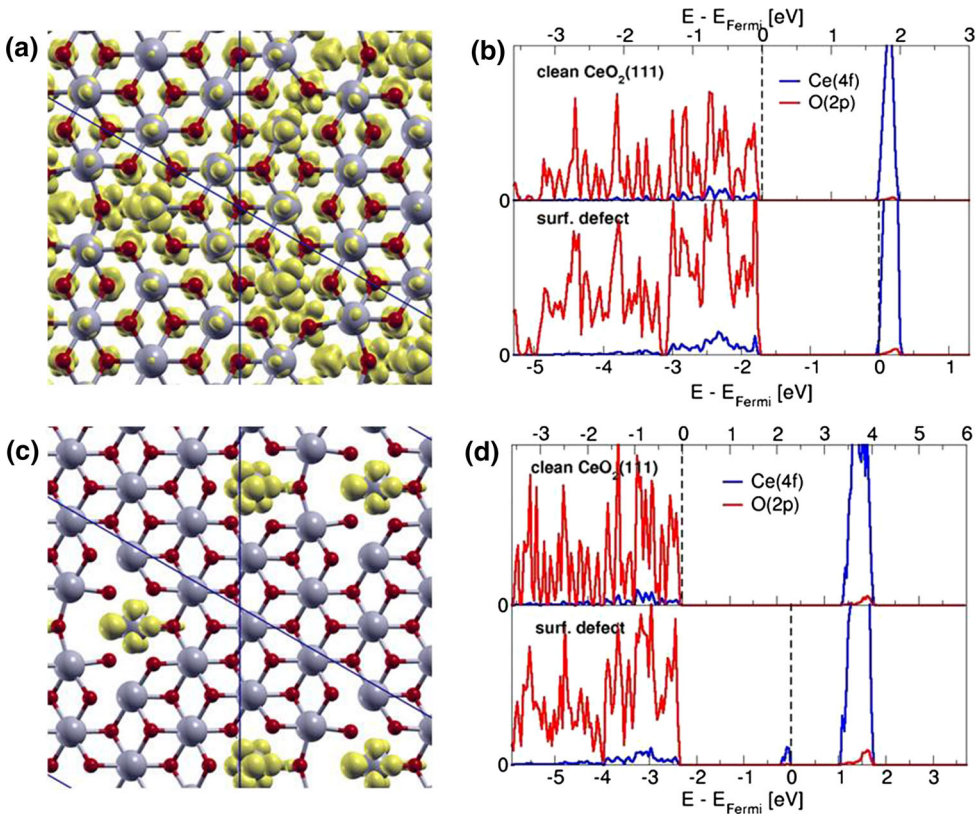

Fig. 1 **a** Spin-densities (*yellow*) for a surface O defect in CeO_2(111) obtained using PBE. **b** Corresponding PDOS for the clean surface (*top panel*) and O defect (*bottom panel*). *Blue lines* indicate the Ce 4f states, and *red lines* indicate O 2p states. **c** and **d** Analogous graphs showing spin-densities as well as PDOS obtained using the hybrid functional HSE (see below). For results on the (110) and (100) surfaces, see [46] and [47]. Reprinted and adapted with permission from [29]. Copyright (2013) American Chemical Society

of water on the Fe_3O_4(111) surface. We survey limitations of hybrid functionals and conclude with final remarks on potential future developments.

1.1 Jacob's Ladder of Density Functional Approximations

It is frequently stated that DFT does not offer possibilities to systematically improve the accuracy of results in the way, e.g., wavefunction-based techniques do [48–57]. "Jacob's ladder of density functional approximations" [58, 59] is an attempt to introduce, at least to a certain extent, the aforementioned systematics. Currently the ladder comprises five rungs or classes of approximations. The underlying idea is that functionals accommodating a number of physical or exact constraints, e.g., meeting the uniform electron gas (UEG) limit for vanishing density gradients, are expected to be rather universally applicable and transferable. This means that the accuracy of results does neither critically depend on the material nor on the calculated property. The number of satisfied constraints or degree of complexity increases for higher rungs, but the amount of empiricism used for their construction should be minimal to avoid "overfitting" [60]. This way, the functionals' accuracies are expected to improve using higher rungs on the ladder.

LDA and GGA are known as the first and second rung on the ladder. The third rung refers to the meta-GGA approximation [61], which is on the point of becoming widely recognized in the catalysis community [62–66]. LDA, GGA, and meta-GGA are pooled by the term *semilocal* functionals, because of their dependence on the local electron density $\rho(\mathbf{r})$ as well as on derivatives of $\rho(\mathbf{r})$. While LDA only depends on ρ (including spin-polarisation [67]), GGA also incorporates information on the reduced density gradient, which is proportional to $\frac{|\nabla\rho|}{\rho^{4/3}}$ [68–72]. A meta-GGA, in addition to its dependence on density and density gradient, includes information that originate from the kinetic energy density [73]. The information contained in the latter was shown to be almost equivalent to the one carried by the second derivative or the Laplacian of the density [74].

The fourth rung functionals contain also non-local information due to the explicit dependence on the occupied orbitals. In theory, this requires developing a generalization of KS-DFT [75]. In practice, this means that a fraction of non-local Fock exchange (FX) replaces the corresponding amount of semilocal exchange. The 'mixing ratio' is material-specific and hence a semi-empirical parameter [76–78]. Several hybrid functionals use 20–25 % of FX, which is a useful choice for many materials or systems of

interest. This choice was supported by non-empirical arguments [79], but they turned out to be imprecise [59].

The present work does not discuss hybrid functionals relying on many parameters [80, 81]. With regard to local hybrid functionals employing position dependent admixture of FX, we refer the interested reader to the literature (cf., e.g., [82–84]).

The generalized random-phase approximation (RPA) is the fifth rung on Jacob's ladder (cf., e.g., [17, 85–87]). This rung adds non-locality also in the correlation energy via dependence on occupied as well as virtual orbitals (and orbital energies). Thus, RPA is a fully non-local functional. RPA can be applied to small-gap and metallic systems, in contrast to double-hybrid functionals, which add a fraction of correlation energy based on second order Møller-Plesset perturbation theory (cf. [88–90]). Any 'order-by-order' perturbation theory breaks down when applied to systems with zero gap [91]. RPA describes dispersion-type van der Waals interactions correctly (e.g., [92, 93]). Up-to-date applications of RPA mostly use semilocal orbitals and orbital energies as input (e.g., [17, 94–99]. This also applies to the FX energy expression, which is then called exact exchange (EXX) energy. However, advantages by using the FX energy (i.e. using HF orbitals in the EXX energy expression) were reported by Xinguo Ren and coworkers [100, 101]. Throughout this work, we will not discriminate between EXX and FX. Self-consistent RPA calculations have not yet been applied to extended systems, although the number of recent publications indicate intense research activities [102–108].

2 Historic and Technical Remarks on Hybrid Functionals

Axel Becke introduced hybrid functionals in 1993 [109]. He used arguments based on the so-called adiabatic connection formula [110, 111] to theoretically motivate the employed mixing-ratio, i.e. 50 % of FX and 50 % of Slater-Dirac (LDA) exchange [112, 113]. This hybrid, known as the "Becke-Half-and-Half" (HH) functional, substantially outperformed both HF and LDA with respect to errors in molecular atomization energies. Moreover, the work reports improvements by employing two independent mixing parameters obtained from fitting against experimental data. The modified functional uses a smaller amount of FX (33 %) and sacrifices a constraint, namely the uniform electron gas (UEG) limit [109]. Despite its excellent performance in molecular atomization energies, this parametrization spoiled the accuracy in other properties such as proton affinities.

The three-parameter functional B3PW91 [114] was also introduced by Becke (Eq. 1).

$$E_{xc}^{B3PW91} = E_{xc}^{LDA} + a_0 \cdot \left(E_x^{FX} - E_x^{LDA}\right) + a_x \cdot \Delta E_x^{B88} + a_c \cdot \Delta E_c^{PW91} \quad (1)$$

It outperformes HH in terms of molecular atomization energies and preserves the UEG limit. The three parameters in Eq. 1 refer to the admixing factors for FX ($a_0 = 0.2$), the Becke-88 (B88) [115] gradient-correction to the LDA exchange ($a_x = 0.72$), and the Perdew–Wang-91 (PW91) [69, 116] gradient-correction to the LDA correlation energy ($a_c = 0.81$), respectively.

These parameters were fitted to minimize errors in calculated molecular properties such as atomization energies, ionization potentials, etc. Note that the popular B3LYP hybrid functional finds its origin in B3PW91, replacing LDA correlation together with PW91 gradient corrections by the Lee–Yang–Parr (LYP) correlation functional [117]. LYP consists of density dependent (local) terms as well as gradient-dependent (semilocal) contributions [118]. B3LYP was employed and published by Mike Frisch und coworkers for the first time in 1994 [119].

LYP is based on the Colle-Salvetti (CS) functional and does not fulfill the UEG limit. For vanishing density gradients, it lacks some of the correlation energy compared to LDA [120, 121]. As discussed in [122], electron correlation at the short range, i.e. small inter-electron distance, is less affected. However, at the long range, the effect of the aforementioned failure becomes noticeable. It is less problematic for calculations on atoms and molecules, but for solids errors may be significant. This shortcoming of LYP is nicely depicted in Fig. 5 of Ref. [120].

Figure 2 shows atomization energies for several archetypal metals, semiconductors, and insulators obtained with the Perdew, Burke, Ernzerhof (PBE) GGA [70] and the Heyd, Scuseria, Ernzerhof (HSE, vide infra), B3PW91, as well as B3LYP hybrid functionals [123]. The large negative relative errors illustrate the failure in LYP when

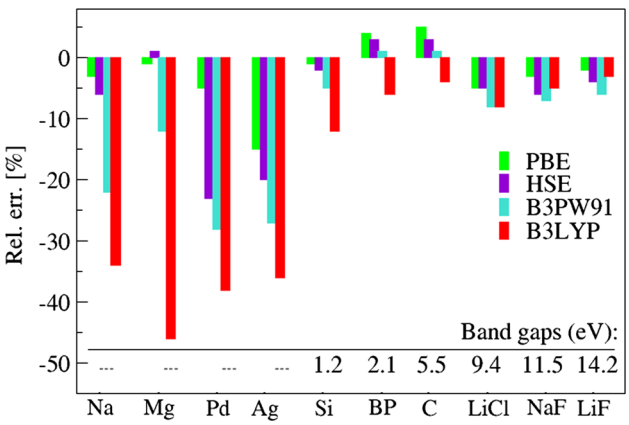

Fig. 2 Relative errors in atomization energies (theory minus experiment) obtained using PBE (*green*), HSE (*violet*), B3PW91 (*light blue*), and B3LYP (*red*) [123]

applied to electron–gas-like systems, i.e. metals. The systematic underestimation of atomization energies can be readily understood. Supposed that the calculations for the atoms are reasonably accurate, the stability of the bulk material is underestimated by B3LYP, very likely due to the underestimation of correlation for the UEG described above. As indicated by the pronounced error bar for Si, problems also arise for small gap semiconductors, featuring delocalized orbitals or a slowly decaying density matrix [124]. For B3PW91, which fulfills the UEG limit, errors in metallic systems are substantially smaller compared to B3LYP [123]. Except for Na and Mg, B3PW91 and HSE perform similarly.

To avoid errors incurred by LYP and to single out the effect of admixed FX, it is advisable to compare the performance of PBE solely with B3PW91 and HSE. Both hybrids fulfill the UEG constraint. As shown in Fig. 2, admixture of FX yields suboptimal results for metallic systems. This finding is along the lines of, e.g., [65].

The UEG is the prototype model for metallic systems and applying HF to the UEG causes the electronic density of states to vanish logarithmically at the Fermi level [125, 126]. This artifact is a consequence of the long-range nature of the Coulomb $1/|\mathbf{r}_1 - \mathbf{r}_2| = 1/r_{12}$ interaction among electrons (cf. [124]). Two electrons at large distances do not feel the full $1/r_{12}$ potential, but a "screened" version due to the presence of, e.g., the other electrons as an intervening medium. So-called polarization or rearrangement effects of the electron gas cancel out the long-range part of the potential. Therefore, higher-order correlation effects, e.g., within the (non-local) RPA approximation, compensate this singular behavior of the potential [127]. Semilocal approximations to correlation employed in a hybrid functional insufficiently compensate the aforementioned singularity. A body of work in the literature points out the underperformance of hybrid functionals when applied to extended metallic systems [65, 77, 123, 128–130].

Summarizing the discussion on B3LYP, Fig. 2 shows a relation between B3LYP errors in atomization energies and the size of the band gap. Larger band gaps relate to smaller errors. Supposed that all of these functionals are comparably accurate for atoms, this finding is sensible, because the density matrix of wide-gap systems decays rapidly with the distance [15, 131]. It implies a high degree of localization in orbitals [132]. Apparently, the case involving a more localized scenario is unproblematic for the LYP functional. Recalling that B3LYP is plagued by two important shortcomings: (a) the long-range part of FX, which is problematic in metallic systems; (b) LYP does not describe long-range contributions of correlation effects in delocalized (metallic) states accurately. Using B3LYP, both shortcomings add up and lead to conspicuously large error bars for metallic systems as well as for small-gap semiconductors like Si.

In 1996, Becke introduced a simplified one-parameter hybrid functional shown in Eq. 2.

$$E_{xc}^{hybrid} = E_{xc}^{DFT} + a_0 \cdot \left(E_x^{FX} - E_x^{DFT}\right). \quad (2)$$

The admixing factor for FX, a_0, is usually small and varies between 0.16 and 0.28 depending on the GGA exchange functional used (i.e. E_x^{DFT} in Eq. 2) [133]. The popular PBE0 or PBEh hybrid functional is based on the PBE GGA functional and uses 25 % of the FX energy (E_x^{FX}). It was introduced into the literature and independently assessed by Carlo Adamo and Vincenzo Barone [134] as well as Matthias Ernzerhof and Gustavo Scuseria [135]. Both groups reported high accuracy for a broad variety of molecules and their properties.

As mentioned before, the long-range asymptote of the Coulomb interaction (cf. Fig. 3a, black line) renders the application of hybrid functionals to metallic and semiconducting solids with a small band gap numerically difficult. As demonstrated in [77], the slow decay of $1/r_{12}$ with

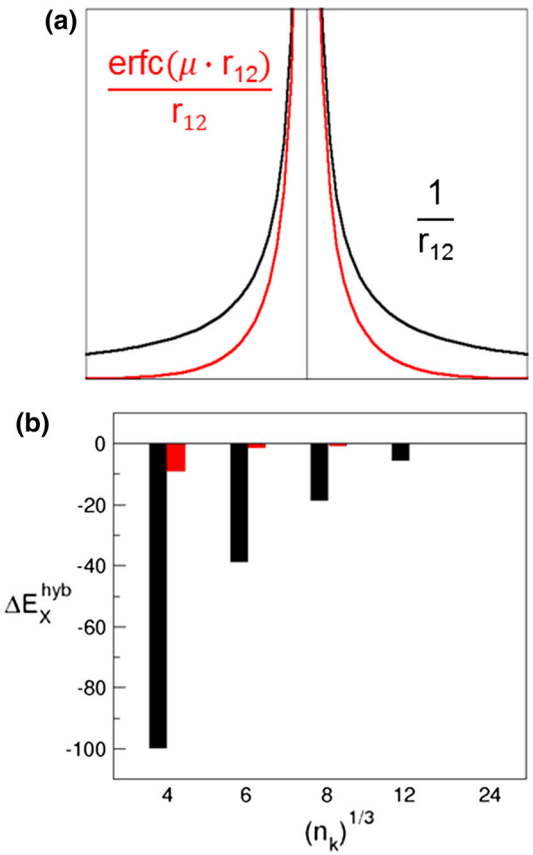

Fig. 3 **a** Decay of a screened (*red*) and unscreened (*black*) Coulomb kernels. **b** Error in the exchange energy ΔE_X of fcc Al with (HSE, *red*) and without (PBE0, *black*) screening as a function of *k* points ($n_k \times n_k \times n_k$). See also [77]

distance requires dense *k*-point grids (or equivalently large supercells) to converge the FX energy.

To remedy this problem, one may resort to screening or range-separation of the Coulomb interaction. In molecular quantum chemistry, this technique was successfully applied to describe short-range correlation using DFT and long-range correlation effects using wavefunction-based methods [136]. In Fig. 3a the screened Coulomb interaction using the complementary error function is shown (Eq. 3).

$$\frac{1}{r_{12}} = \underbrace{\frac{\mathrm{erfc}(\mu \cdot r_{12})}{r_{12}}}_{\mathrm{SR}} + \underbrace{\frac{\mathrm{erf}(\mu \cdot r_{12})}{r_{12}}}_{\mathrm{LR}} \tag{3}$$

In principle, any functions summing up to 1/r are suitable for range separation. A screening based on the error function like in Eq. 3 is advantageous using GTOs or plane waves as a basis set [77, 137]. Historically, the first application of the error function dealt with efficient lattice summations of the long range electrostatic interactions in crystalline solids. It is commonly known as the Ewald technique [138]. The HSE or equivalently HSE06 hybrid functional, defined in Eq. 4, uses range separation in the exchange energy contribution according to Eq. 3 [137].

$$E_{HSE-X} = E_{PBE-X} + a_0\left(E_{FX}^{SR}(\mu) - E_{PBE-X}^{SR}(\mu)\right) \tag{4}$$

In Eq. 4, the superscript "SR" refers to "short-range" and a_0—similar to PBE0—amounts to 25 %. This means that the FX energy (or potential) is evaluated using the short-range kernel of the Coulomb interaction (cf. Fig. 3, red lines). The empirically set parameter μ amounts to 0.207 $\mathrm{Å}^{-1}$ and determines the length scale of the short-range and long-range interactions [139]. This offers substantial computational savings for metallic systems as shown in Fig. 3b [77]. The figure shows respective errors in the FX energy for the fcc bulk phase of Al with (red bars) and without (black bars) range separation as a function of the number *k* points. In other words, the figure compares the aforementioned convergence in the HSE and PBE0 exchange energies. Apparently, range-separation drastically enhances the technical convergence of the energy. HSE is very useful for treating metals and insulators on the same footing [26, 77, 140]. The high accuracy in band gaps obtained with HSE is amply discussed in recent review articles [26, 30, 141].

Hybrid functionals have been commonly used in the field of molecular quantum chemistry almost instantaneously after their introduction by Axel Becke. At the same time, they were offered to the computational solid state community by virtue of the CRYSTAL code [142] using Gaussian-type orbitals (GTOs) as a basis set to expand the crystal orbitals [143, 144]. GTOs are also used in the GAUSSIAN suite of programs [137, 145, 146]. Local (atom-centered) basis functions offer the possibility to treat all electrons, i.e. core as well as valence orbitals in the self-consistent field optimization. However, incompleteness or superposition errors [147, 148] have to be tackled by techniques like, e.g., the Boys-Bernardi counterpoise correction [149].

Hybrid functionals are implemented in many solid state electronic structure codes. The required FX energy can be computed employing various basis sets such as all-electron numeric (localized) orbitals as used in FHI-aims [150, 151] and full-potential linearized augmented plane waves as used in WIEN2K [152, 153] or Fleur [154, 155]). Moreover, projector-augmented pseudopotentials and plane waves are used in VASP [77, 156] or GPAW [157, 158], and mixed basis sets are employed in CP2K [159]. Pseudopotentials and plane waves are used in Quantum ESPRESSO [160, 161] or CASTEP [162–164]. Consequently, hybrid functionals are now accessible to a large manifold of computational communities.

3 Hybrid Functionals and the DFT + U Approach

Both, hybrid functionals as well as the DFT + U approach [165–168] assist in treating localized d or f electrons. The fraction of FX used in a hybrid functional partially alleviates one-electron SIEs in semilocal functionals, thus enhances localization.

Within DFT + U, the orbitals are subdivided into two groups, namely rather delocalized orbitals that form bands and spatially localized, atomic-like orbitals. These groups of orbitals are treated differently. This is justified by the assumption that semilocal functionals describe the band formation within s and p orbitals well, but corrections are required for the other case (d and f orbitals). The Mott–Hubbard theory [169–172] serves as the conceptual basis for DFT + U, relying on the idea of a hindered transfer of electrons among neighboring sites. The electron interaction is described by the Hubbard Hamiltonian involving effective Coulomb (U) and exchange (J) interactions. The meaning of U was extensively discussed by Herring [173]. For instance, in a 3d electron system with n electrons per atom, U is defined as the energy cost involving electron detachment at one site and attachment at a neighboring site, i.e. the 'redox' reaction energy.

Following [174], bypassing above mentioned deficiencies in LDA or GGA requires the introduction of a U-dependent correction to the total energy. The one-electron SIE-free HF theory is used as a reference. The correction to the DFT energy reads

$$\Delta E_{corr}[\{n_i\}] = E^{HF}[\{n_i\}] - E_{dd}^{DFT}[n_d], \tag{5}$$

with $E_{dd}^{DFT}[n_d]$ as the energy contribution stemming from the erroneous DFT description of interacting d electrons.

Equation 5 uses n_i as the occupation number of orbital i and n_d refers to the total number of d electrons, i.e. $n_d = \Sigma_i n_i$. The HF energy expression, with $E^{HF}[\{n_i\}]$ as a functional depending on the set of d orbitals, reads

$$E^{HF}[\{n_i\}] = \frac{e^2}{2}\sum_{i\neq j}(U_{ij} - J_{ij})n_i n_j, \tag{6}$$

with U_{ij} and J_{ij} as orbital-dependent Coulomb and exchange integrals. To illustrate the working principle, the electron exchange term J in Eq. 6 can be neglected [174], which leads to a simplified expression for the correction

$$\Delta E_{corr}[x] = -\frac{1}{2}Ux(x-1), \quad 0 \leq x \leq 1, \tag{7}$$

with x as the variation of the total number of d electrons [174]. This expression involves a $E_{dd}^{DFT}[n_d]$ of similar structure (see [174]). In consequence, the corresponding correction to the one-electron potential is equal to

$$\Delta V_{corr}[x] = \frac{d\Delta E_{corr}}{dx} = U\left(\frac{1}{2} - x\right). \tag{8}$$

Equations 7 and 8 convey the essential physics underlying the DFT + U approach. Supposing a half-filled d orbital, the correction to the total energy will result in a maximal increase in energy, whereas the correction to the Kohn–Sham eigenvalue vanishes. Conversely, integer occupation will be (variationally) preferred by the orbital-dependent DFT + U functional, which in turn leads to the opening of the band gap (Eq. 8). Unoccupied orbitals (x = 0) will be shifted by $+^1/_2$ U and occupied orbitals (x = 1) will be lowered by $-^1/_2$ U (cf. Fig. 4). Localization of d or f electrons is therefore inherent to DFT + U,

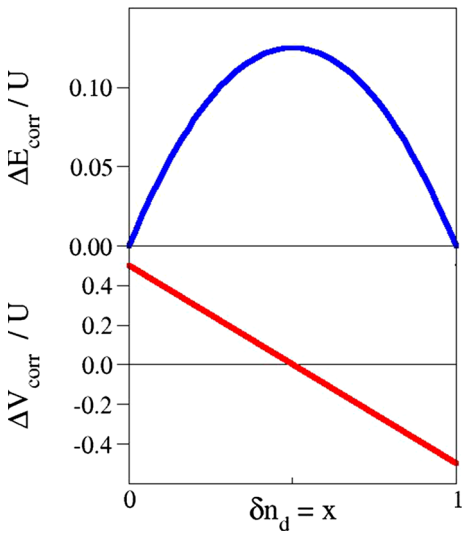

Fig. 4 Correction to the total energy (ΔE_{corr}, *blue line*) and the potential (ΔV_{corr}, *red line*) within DFT + U as a function of the variation of *d* orbital occupation x. See also [174]

which incorporates orbital-dependence in a somewhat less rigorous manner compared to HF theory. Using a hybrid functional, all occupied orbitals are subject to the same generalized Kohn–Sham Hamiltonian [75], whereas in DFT + U only a subspace of orbitals is corrected in the aforementioned *ad hoc* manner. In practical applications, the size of U matters. It is usually chosen in a way to trade off the accuracy in the band gap against the accuracy reached for other system properties such as lattice parameters or reaction energies (e.g., [175–177]). Applying U together with semilocal functionals leads to increased lattice parameters. This is beneficial for LDA, because it underestimates lattice constants, but unfavorable for GGA functionals like PBE, which overestimate them [8]. For further discussions on DFT + U, we refer the interested reader to the literature [29, 178, 179].

4 Case Studies

4.1 Methanol Oxidation at Vanadia Supported on Ceria

Ceria as a support material for transition metal oxides like, e.g., vanadia has attracted much interest in the field of heterogeneous catalysis. Depositing vanadia on a ceria surface drastically increases turnover frequencies for the methanol oxidation to formaldehyde [180, 181]. The turnover frequencies for supported vanadia may vary within a range of three to four orders of magnitude depending on the nature of the support, i.e. its reducibility [29]. Importantly, it may also depend on the preparation of the catalyst (see, e.g., [182]). The vanadia coverage or loading also affects reactivity [183, 184]. Catalysts prepared by choosing amounts of vanadia lower than or equivalent to the so-called monolayer coverage are significantly more active than those with loadings large enough to form V_2O_5 nanoparticles [185, 186]. Precise atomic level details underlying the observed reactivity are generally missing, which induced a drive to generate these details by virtue of first-principles DFT studies.

In this section, we report the results of an extensive study on a $VO_x/CeO_2(111)$ catalytic model system [184, 187–190] examining the selective oxidation of methanol for low vanadia coverage on a ceria surface under dehydrated conditions. We compare kinetic results, i.e., intrinsic reaction barriers obtained using DFT + U and hybrid functionals with temperature-programmed spectroscopy (TPS) analyzed using Redhead's equation [191].

Previous collaborative efforts between the groups of Hajo Freund and Joachim Sauer in Berlin generated crucial insights into the atomic structure of the submonolayer vanadia catalyst deposited on a $CeO_2(111)$ surface [187]. These systems were investigated by applying surface

science techniques, such as atomically resolved scanning tunneling microscopy (STM), infrared absorption spectroscopy (IRAS), X-ray photoemission spectroscopy (XPS), TPS, as well as DFT. Vanadia was grown on a well characterized $CeO_2(111)$ film on a metal substrate by virtue of physical vapor deposition of metallic vanadium in an oxygen atmosphere. These studies give rise to the following main conclusions: (i) VO_x wets the support in a two-dimensional manner (Fig. 5) according to the constant apparent height of the occupied state STM images as well as DFT calculations [188]. (ii) Each VO_x cluster is terminated by V=O, i.e., vanadyl bonds as evidenced by IR and DFT. (iii) Larger VO_x agglomerations such as trimers (Fig. 5b) are created upon sintering of larger amounts of vanadia at 700 K. (iv) V=O dipole moments couple within these clusters, leading to a blue shift of the IR-active resonance of the V=O stretching mode. This blue shift was reproduced by DFT calculations [187, 188]. A structure-IR relationship was corroborated by the computational results: the larger the VO_x clusters, the larger the blue shift in IR wavenumbers. (v) XPS indicates occupied Ce 4f orbitals in agreement with DFT. Each VO_x cluster at the $CeO_2(111)$ surface contains one tetrahedrally coordinated V atom in its highest oxidation state (+5). Ce atoms accommodate the 3d electrons of V in one of the 4f orbitals, i.e. upon V deposition and oxidation, some Ce^{4+} ($4f^0$) ions are reduced, thereby creating Ce^{3+} ($4f^1$) ions.

However, the composition of the VO_x clusters at the $CeO_2(111)$ surface was unknown. This question could be successfully answered by DFT + U calculations combined with ab initio thermodynamics [192]. These calculations use the PBE GGA xc functional and a U parameter of 4.5 eV for the Ce 4f orbitals. This U value for Ce 4f was calculated self-consistently by Fabris et al. [193]. It was found that under the relevant, slightly reducing conditions, VO or VO_2 originating from the gas phase represent the prevalent surface species [189]. This finding was confirmed by Paier et al. [194] for low coverage using a larger surface unit cell than the one applied in [189].

Thermodynamic stabilities of various VO_x oligomers and their respective reactivities were addressed by Penschke et al. using PBE + U [188]. The calculated structures of VO deposited at $CeO_2(111)$ as well as oligomers of VO_2 units on that surface are depicted in Fig. 6. This is the way how the VO_x catalyst is modelled: uncharged VO with V featuring a $3d^3$ occupation, and VO_2 with V ($3d^1$) are put on the clean $CeO_2(111)$ surface. Figure 5 shows the optimized, minimum-energy structures, where the previous V 3d electrons are spontaneously transferred into Ce 4f orbitals. As a consequence, VO shows three Ce^{3+} ions (dark blue), and VO_2 features one Ce^{3+} in the surface. Note that the cutout in Fig. 6 does not show the Ce^{3+}, because it is located farther away from the VO_2 moiety [188].

Trimerization of VO monomers at the surface requires 333 kJ/mol (PBE + U). Thus, agglomeration of VO into $(VO)_3$ trimers is thermodynamically unfavorable. In contrast, deposited VO_2 monomers were found to trimerize pronouncedly exothermically releasing 162 kJ/mol. Experimentally, after slight sintering at higher loadings, trimers were found to be fairly abundant surface species [187]. This finding is consistent with the highly exothermic trimerization of VO_2. Calculated vibrational properties of $(VO_2)_3$ also agree with the observation. Particularly, the observed blue shift of of 27 cm^{-1} for the V=O stretching mode agrees excellently with the calculated value (25 cm^{-1}). With regard to oxidation states, the remaining V ($3d^1$) electron of the VO_2 cluster is always transferred into a Ce 4f orbital upon adsorption on the surface. Therefore, a single Ce^{3+} cation is created per VO_2 unit and V adopts its highest oxidation state +5. A minimum energy $VO_x/CeO_2(111)$ structure featuring (partially) reduced V could not be found [187–189, 194]. With respect to the oxidation state of vanadium, similar findings were obtained for mixed V/Ce-oxide clusters [195, 196]. Concerning surface structures, V is fourfold

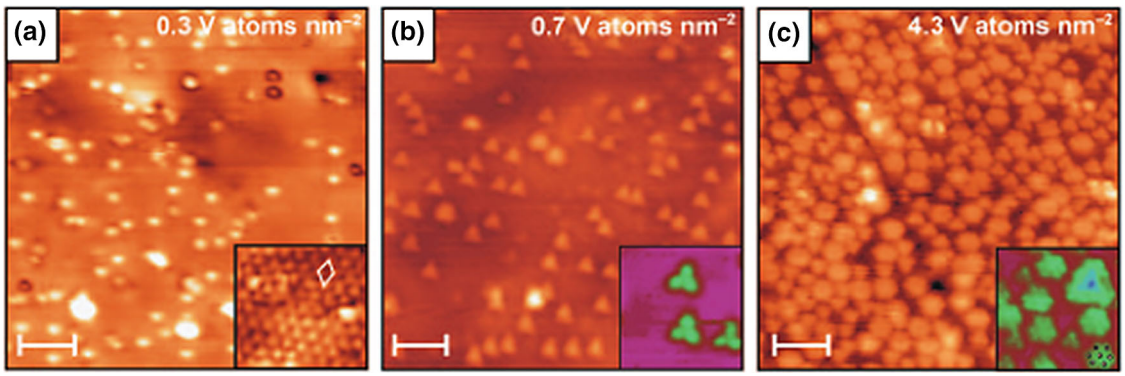

Fig. 5 STM images of VO_x species at the $CeO_2(111)$ surface showing **a** monomers, **b** trimers, and **c** larger oligomers for loadings corresponding to 0.3, 0.7, and 4.3 V atoms/nm^2, respectively. Adapted with permission from [187]. Copyright (2009) John Wiley and Sons

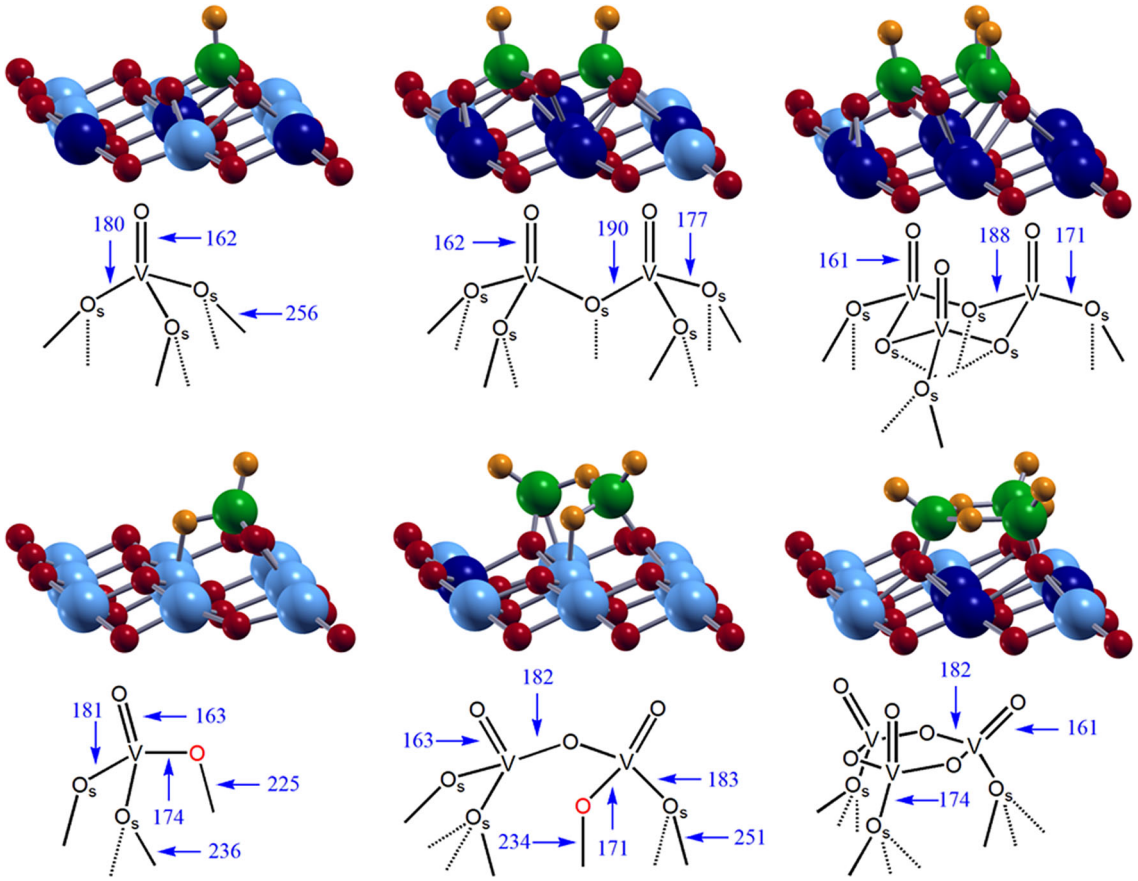

Fig. 6 Minimum energy structures of VO (*top*) and VO_2 species (*bottom*) represented as ball and stick models. For clarity reasons only a (3 × 3) cutout of the first O–Ce–O trilayer is shown (Ce^{4+} *light blue*, Ce^{3+} *dark blue*, V^{5+} *green*, O^{2-} in the surface *red*, O^{2-} from the *gas phase orange*). Corresponding schemes are given below with bond distances in pm. The "special" O atom in VO_2 and V_2O_4 is highlighted in *red* and "O_s" refers to a surface O. Adapted from [194]

coordinated by oxygen atoms resulting in a slightly distorted tetrahedron. To achieve this coordination for the VO_2 deposited on $CeO_2(111)$, two more oxygen ions from the terminating surface oxygen layer are needed.

But what about the reactivity of $VO_x/CeO_2(111)$? To answer this question, we focus on the TPS spectrum recorded for the oxidation of methanol to formaldehyde on mononuclear VO_x species on ceria [184]. Formation of these surface species requires low V loadings (cf. STM shown in Fig. 7).

The TPS spectrum of $VO_x/CeO_2(111)$ is markedly different from the one of the clean surface. A so-called α peak of desorbing formaldehyde centers at about 370 K. This desorption temperature (T_{des}) is much lower than T_{des} of the γ peak, which is characteristic for the clean $CeO_2(111)$ surface ($T_{des} \sim 570$ K). Employing the Redhead formula [191] based on a heating rate of 3 K s^{-1} and a pre-exponential factor of 10^{13} s^{-1}, the corresponding desorption barriers for α and γ have been estimated and amount to 100 kJ/mol and 150–160 kJ/mol, respectively [184]. Thus, deposition of mononuclear vanadia clusters on $CeO_2(111)$ drastically enhances the dehydrogenation activity of the ceria support.

To understand this observation, individual mechanistic steps, i.e. possible minimum energy pathways for the dehydrogenation of methanol adsorbed on the clean $CeO_2(111)$ surface (fully oxidized and reduced) [197] and on the $VO_x/CeO_2(111)$ [190] system were studied with PBE + U and the HSE hybrid functional including the Grimme D2-type dispersion correction [198, 199]. For the $VO_x/CeO_2(111)$ surface additional calculations using the B3LYP hybrid functional were accomplished [190]. This was carried out having the well-defined surfaces under UHV conditions in mind. Prior to the TPS experiments, the surfaces were pre-saturated by dosing methanol. For low methanol coverage, dissociative adsorption occurs [197, 200]. Hence, observed desorption temperatures correspond to intrinsic barriers involved in the oxidation of the adsorbed methoxide. As a consequence, a comparison of theory with experimental results appears to be optimally suited to check whether observed and calculated activation barriers agree.

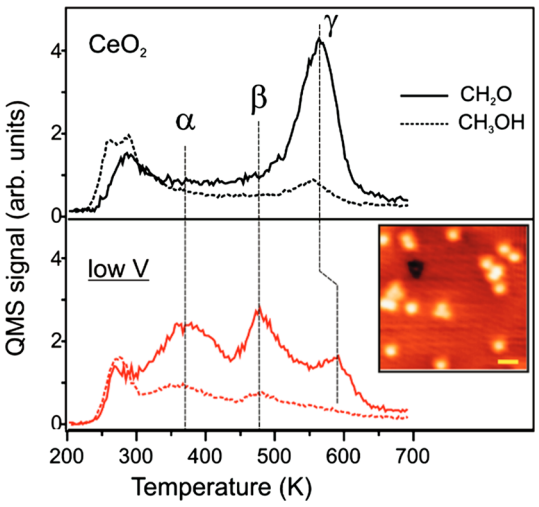

Fig. 7 TPS for ~5 L of CH_3OH adsorbed at 300 K on $CeO_2(111)$ (*upper panel*) and $VO_x/CeO_2(111)$ surfaces (*lower panel*) for a low loading of vanadia (<2 V/nm^2). The *inset* shows a typical STM image at the respective coverage. Reprinted and adapted with permission from [184]. Copyright (2010) American Chemical Society

Calculations for methanol adsorbed on the O-defect-free $CeO_2(111)$ surface suggest, that methanol prefers to desorb, instead of being oxidized to formaldehyde [197, 201, 202]. This is corroborated by the desorption energy of 88 kJ/mol compared with the substantially larger activation barrier for the oxidation step of 104 kJ/mol. In contrast, surface O-defects in $CeO_2(111)$ are reactive sites for the methanol oxidation. Here, the methoxy binds in the vacant site with 230 kJ/mol obtained using PBE + U + D. This value is slightly overestimated compared with the supposedly more accurate binding energy of 206 kJ/mol obtained using HSE + D. The PBE + U + D reaction barrier amounts to 129 kJ/mol, which is slightly higher than the barrier for the pristine surface. The HSE + D barrier at the defect is higher by only 10 kJ/mol. Given the strongly exothermic adsorption at the vacancy, this barrier can be easily overcome (cf. Fig. 5 in [197]).

Experimentally, it is known that the activity in TPS, i.e. peak intensity, increases with an increasing number of O defects in the surface [203, 204]. This is consistent with the findings given above: the more vacancies in the surface, the more methoxide will be converted to formaldehyde giving rise to higher intensities in TPS desorption peaks. The above mentioned HSE + D barrier of 139 kJ/mol agrees very well with the barrier suggested by TPS and Redhead analysis (~150 kJ/mol) [184].

To get fast insight into the reactivity of VO_2 on ceria, O-defect formation as well as hydrogenation energies were calculated [188]. As shown in [42] and [205], these are appropriate reactivity descriptors for reactions following a Mars-van Krevelen mechanism [41]. The O-defect formation energy, which corresponds to the overall reaction energy, and the hydrogenation energy, which relates to the barrier of the C–H bond breaking, are therefore valuable descriptors for the methanol oxidation on supported metal oxides. According to PBE + U results, a single VO_2 on the $CeO_2(111)$ surface is the most promising candidate for the active site.

It is interesting to compare results with vanadia deposited on a non-reducible silica support [206]. Previously, Joachim Sauer and coworkers studied the methanol oxidation step for vanadia supported on silica. In order to do that, silsesquioxane clusters were employed to model the silica surface. The transition state found involved the H-atom transfer from the methoxy towards the nearby V=O bond forming a five-membered ring, very similar to the analogue transition structure for vanadia on ceria (**TS1**, cf. Fig. 8). This work concludes that the reaction barrier obtained using B3LYP within the broken-symmetry approach [207], required for biradicaloid systems, is too high. This was shown by comparing results obtained with single-point energy calculations using CCSD(T) [208, 209] and B3LYP for the $O=V(OCH_3)_3$ molecule. The CCSD(T) correction to the B3LYP dehydrogenation barrier (191 kJ/mol, cf. Table 1) amounts to 16 kJ/mol. Hence, the B3LYP barrier corrected by the ΔCCSD(T) decrement is 175 kJ/mol. The above mentioned findings for the non-reducible silica support are instructive, because silica remains "electronically innocent" in the course of the reaction.

The same pathway (among others), i.e. H-atom transfer from the methyl group to the vanadyl O-atom, was studied for $VO_2/CeO_2(111)$ [190]. Similar to the transition state found for the silica support, no electrons were transferred to

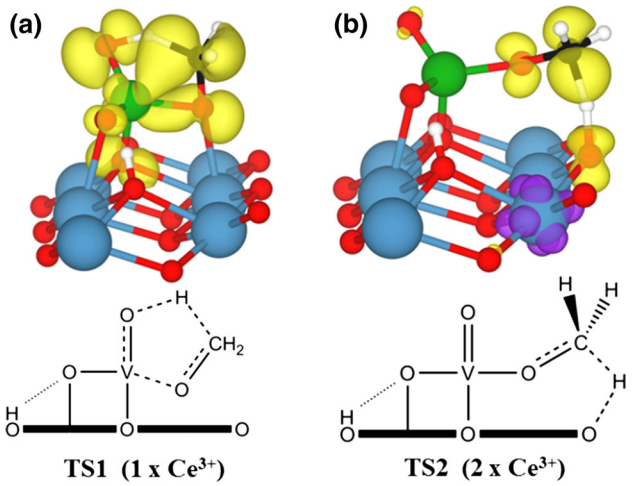

Fig. 8 Electron and spin density (positive: *yellow*; negative: *purple*) contour plots at 0.01 Å^{-3} showing the frontier orbitals involved in the formation of transition state **TS1 a** and **TS2 b**. Total number of Ce^{3+} ions in the $CeO_2(111)$ surface is given in the schemes below. Reprinted and adapted with permission from [190]. Copyright (2014) American Chemical Society

Table 1 Intrinsic barriers (kJ/mol) corresponding to transition states **TS1** and **TS2** (cf. Fig. 8) for the oxidation step of methoxide at vanadia/ceria and vanadia/silica, respectively

	TS1		TS2
	VO_x/SiO_2	VO_x/CeO_2	VO_x/CeO_2
PBE + U		169[a]	120[a]
HSE		177[a]	150[a]
B3LYP	191[b]	198[a]	149[a]
B3LYP + ΔCCSD(T)	175[b]	182[c]	

[a] Ref. [190]

[b] Ref. [206]

[c] Obtained from the barrier in Ref. [190] subtracting ΔCCSD(T) = 16 kJ/mol as calculated in [206]

the surface, thus no additional Ce^{3+} cations were formed upon H-abstraction. The electrons remained on the five-membered ring delocalized over its constituent atoms (**TS1**, Fig. 8) [190]. The barrier for the oxidation step found employing B3LYP subject to periodic-boundary conditions [123] amounts to 198 kJ/mol (cf. Table 1) and is very similar to the dehydrogenation barrier on a silica support. Subtracting the ΔCCSD(T) correction of 16 kJ/mol gives a barrier of 182 kJ/mol. This value agrees very well with the HSE barrier of 177 kJ/mol. Thus, we believe that the HSE barrier is accurate.

In contrast, the PBE + U barrier (169 kJ/mol) involving **TS1** having electrons delocalized over the five-membered ring, agrees fairly well with the HSE result. One may conclude that PBE + U performs well in case of rather nonpolar transition states involving a delocalized charge density.

For the $VO_x/CeO_2(111)$ system, a large number of distinct adsorption structures and pathways for the H-transfer in the oxidation step were studied [190]. One of them involves the methoxy bound to vanadium, i.e. the methoxide inserted into an "anchoring" V–O bond. This adsorption complex may be dehydrogenated passing through transition structures **TS1** or **TS2** (cf. Fig. 8). The H atom from the methyl group may be transferred to a surface oxygen, which leads to **TS2**. In this pathway, an electron localizes in Ce 4f orbitals close to the vanadia. In contrast to **TS1**, **TS2** shows a spin-density contour indicating a rather localized electronic structure. As outlined in Sect. 3, B3LYP is expected to perform well for situations involving localized charge densities. Indeed, B3LYP and HSE results are de facto identical for the **TS2** barrier. PBE + U is expected to suffer from SIEs in the "localized case". The conjecture is corroborated by the PBE + U barrier of 120 kJ/mol, which is too small compared with results obtained using HSE or B3LYP.

Eventually, the low temperature desorption (α) peak in the TPS shown in Fig. 7 remains to be understood. A pathway involving a low barrier of approximately 100 kJ/mol was reported in [190]. It requires adsorption of the methanol at the so-called pseudovacancy, i.e. a cavity opened in the $CeO_2(111)$ surface upon adsorption of VO_2 [188, 194]. In the oxidation step, the H atom from the methyl group is transferred to the V–O-Ce "interphase" oxygen atom connecting the VO_2 with the surface. The hybrid functional calculation on the corresponding transition structure was not done, but an error estimate from the difference in PBE + U and HSE barriers for **TS2** (i.e., "localized electrons") was computed. The correction amounts to 30 kJ/mol. Adding this correction to the PBE + U barrier of the aforementioned pathway yields a final barrier of 100 kJ/mol. This result agrees excellently with observation. We confirm what is known from molecular quantum chemistry but rarely achieved for reactions on crystalline surfaces due to the computational workload involved. Hybrid functionals clearly outperform DFT + U in terms of activation barriers.

4.2 Adsorption of Gold Atoms on Ceria Surfaces

Gold nanoparticles adsorbed on metal oxides have been intensely studied, since the days Haruta discovered their unexpectedly high activity in low-temperature CO oxidation [210, 211]. Generally, the atomic and electronic structure details of the interface between noble metals such as Au and Pt and the oxide support is crucial for understanding the activity of the catalyst [212–214]. One aspect of these details, so-called metal-support interactions, is of particular importance. These interactions may decisively determine reactivity, as reported in the literature [215–217].

Because of its high reducibility, ceria is a non-innocent support material for noble metals. Observed high catalytic activities were explained by two cooperative factors: (i) electron or charge transfer from the metal to the ceria support, and (ii) oxygen spillover from the support to the metal, i.e. oxidation of the metal [218]. Due to the propensity of ceria to form O defects [27, 29], these sites will play a role, particularly with respect to binding, e.g., single Au adatoms or Au atoms located on the rim of nanoparticles. Every (electroneutral) O defect in the surface is associated with two Ce^{3+} ions. Thus, Ce^{3+} is a mediator in electron transfer processes involved in metal-ceria support interactions. Consequently, polaron hopping can affect the electron-transfer mechanism (cf. [219] and references therein).

The interaction between Au atoms and the surface O vacancy in the $CeO_2(111)$ surface was profoundly studied by DFT + U [220–222] and amply reviewed by Zhang et al. [223]. It was found that the electron from neighboring Ce^{3+} ions is spontaneously transferred into the Au 6s orbital, i.e. Ce^{3+} is reoxidized and the Au^0 is reduced, thereby creating Ce^{4+} and Au^-. The latter binds in the

vacancy with a large binding or adsorption energy of *ca.* 2.6 eV, because of attractive electrostatic interactions.

Ce^{3+} ions were considered as potential adsorption sites for Au adatoms [224]. This was achieved by preparation of a reduced $CeO_2(111)$ surface containing O vacancies in subsurface position of the terminating O-Ce–O trilayer [224]. Annealing conditions, particularly the oxygen partial pressure, determine whether a surface or a subsurface O vacancy is created. After annealing to 1000 K, the density of subsurface defects was $\sim 5 \times 10^{12}$ cm^{-2} [224]. Subsequent dosing of low amounts of Au by virtue of physical vapor deposition, induced the formation of pairs with Au–Au distances commensurate to the lattice of the $CeO_2(111)$ surface. 40 % of the pairs had a distance equal to twice the lattice parameter of the $CeO_2(111)$ surface unit cell ($\sim$7.6 Å, cf. Fig. 9a). The smallest Au–Au distance ($\sim$4.8 Å) was substantially larger than the distance typical of the Au_2 bond ($\sim$2.5 Å [225]). These Au pairs were metastable species, because a 3.0 V pulse via the STM tip rearranged them into upright standing Au_2 dimers. In some cases, the subsurface O vacancy in close proximity to Au was identified by its characteristic STM image (cf. Fig. 1 in [224]). Thus, it was conjectured that formation of the Au pairs is causally related to the Ce^{3+} ions associated with subsurface O vacancies. Paired Au atoms as well as some of the isolated monomers, showed a halo-like contrast in STM images recorded at low bias. This contrast is typical of *charged* metal adatoms when adsorbed on metal oxides like, e.g., alumina [226] or magnesia [227].

Various adsorption configurations for an Au atom in the O-defective $p(2 \times 2)$ surface unit cell were studied using the HSE and B3LYP hybrid functionals (cf. Fig. 9b). The surface contained a single O vacancy in subsurface position, which corresponds to a defect concentration of *ca.* 200×10^{12} cm^{-2}. Four adsorption structures were found. It was shown that electron transfer from a Ce^{3+} $4f^1$ into Au^0 $6s^1$ leads to more stable structures relative to Au in O atop or bridging positions. The latter sites do not yield Au^-, but preserve the Au^0 oxidation state (cf. Fig. 10). The thermodynamic preference of Au^- relative to Au^0 amounts to *ca.* 0.09 eV, when the Ce^{3+} in subsurface position is reoxidized. This means that the final adsorption state is an Au^- ion adsorbed on top of a Ce^{3+} ion.

The stability of structures involving an Au^- ion is caused by large relaxation effects upon oxidation of the Ce^{3+}. As discussed in [29], Ce^{3+} has a larger ionic radius than the Ce^{4+} cation and electron transfer from Ce^{3+} to Au^0 relieves some of the surface strain induced upon O defect formation. Reoxidation of Ce^{3+} to Ce^{4+} involves pronounced stabilizing relaxation in the surface. Au^- ions formed upon oxidation of Ce^{3+} located in the surface or subsurface layer of the reduced $CeO_2(111)$ surface were recently confirmed [228] to be very stable species. The latter work also uses a $p(2 \times 2)$ cell and reports a fifth, distinct adsorption structure with Au located at the hollow site atop a subsurface O. Also for this configuration electron transfer from the Ce^{3+} in subsurface position to Au^0 occurs and the Au^- resides as a nearest neighbor to the surface Ce^{3+}. This structure is almost 0.5 eV more stable relative to the O-atop position [228].

In a next step, a number of Ce^{3+} pair configurations in the larger $p(4 \times 4)$ surface unit cell of the $CeO_2(111)$ surface containing a single subsurface O vacancy were generated (cf. Fig. 9c). The structures were optimized using the HSE hybrid functional and corresponding defect formation energies are presented in Table 2. These results show that the stability of the O defect strongly depends on the particular Ce^{3+} pair configuration. The nearest-neighbor sites of the vacancy, i.e. $\mathbf{a_1}$–$\mathbf{a_3}$ (cf. Fig. 9c), are thermodynamically unfavorable [229, 230]. In contrast, the $\mathbf{b_1}$–$\mathbf{b_3}$

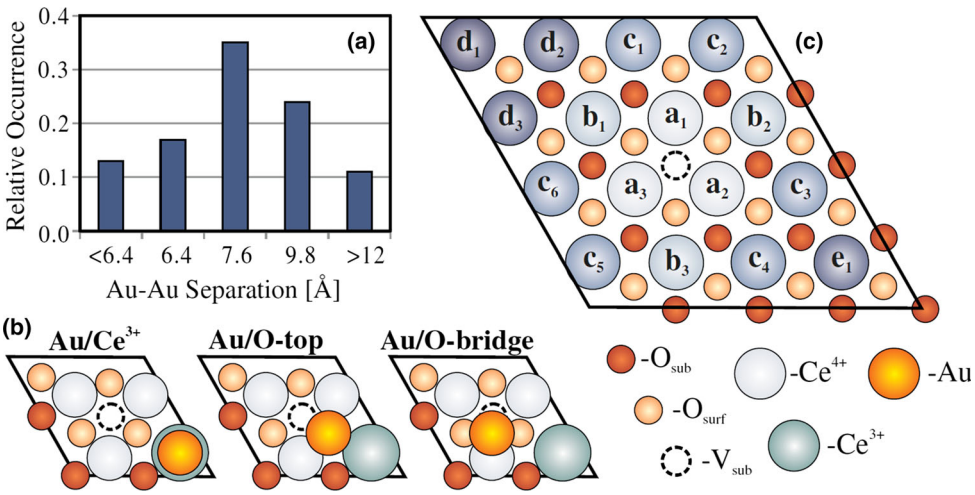

Fig. 9 **a** Distance histogram determined for *ca.* 150 Au pairs on the ceria surface. **b** Configurations of a single Au adatom on reduced $CeO_2(111)$ containing a subsurface O vacancy in a $p(2 \times 2)$ unit cell. **c** Labels indicating the Ce coordination shells in a $p(4 \times 4)$ unit cell relative to the vacant site (cf. Table 2). Reprinted with permission from [224]. Copyright (2013) American Physical Society

Table 2 Structure and vacancy formation energy (E_{def}) with respect to $^1/_2O_2$ for different subsurface O vacancy/Ce^{3+} configurations obtained with HSE [224]

Ce^{3+} configuration	Ce^{3+}–Ce^{3+} distance (Å)	Ce^{3+}-defect distances (Å)	E_{def} ($^1/_2O_2$) (eV)	
			High spin	Low spin
b_1–b_3	7.67	4.41; 4.42	2.32	2.27
a_1–b_3	6.77	2.33; 4.44	2.43	2.41
b_3–c_6	6.65	4.41; 5.84	2.41	
a_3–b_3	3.89	2.34; 4.43	2.50	2.54
b_3–d_3	10.11	4.40; 7.94	2.47	
c_5–c_6	3.88	5.84; 5.85	2.69	
c_1–c_6	7.66	5.85; 5.84	2.66	
a_1–d_3	7.63	2.35; 7.93	2.62	
a_3–c_5	3.77	2.32; 5.86	2.63	
a_1–a_3	4.08	2.37; 2.37	2.71	2.71

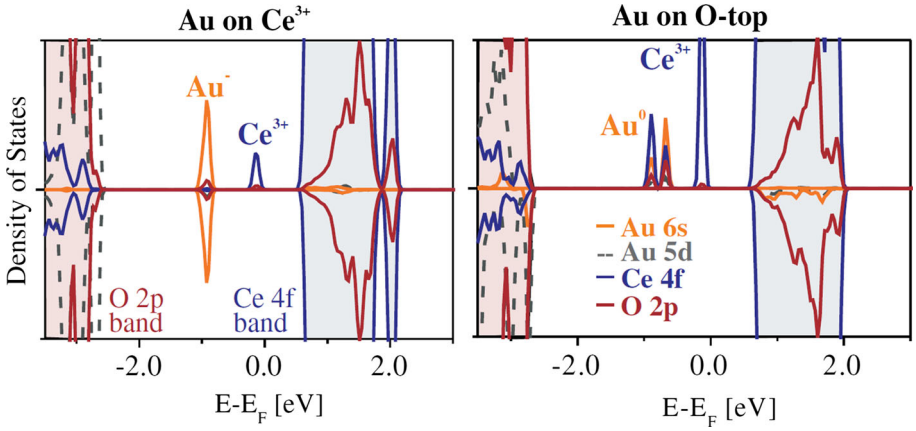

Fig. 10 Respective projected local densities of states obtained with HSE for an Au^- ion bound to a surface Ce^{3+} (left) and to a O^{2-} in atop position (right) in a $p(2 \times 2)$ cell of $CeO_2(111)$. Reprinted with permission from [224]. Copyright (2013) American Physical Society

configuration of two Ce^{3+} ions (i.e., the second cationic shell with respect to the vacancy) is *ca.* 0.40 eV more stable than the $\mathbf{a_1}$–$\mathbf{a_3}$ configuration. The distance between Ce^{3+} ions in $\mathbf{b_1}$–$\mathbf{b_3}$ is equal to two lattice parameters of the $CeO_2(111)$ surface unit cell. The low spin (antiferromagnetic) state is 0.05 eV more stable than the high spin (ferromagnetic) ordered $\mathbf{b_1}$–$\mathbf{b_3}$. Effects induced by the magnetic order are therefore considered as negligibly small. Thus, the favorable stability of Au^- created upon electron transfer from surface or near-surface Ce^{3+} together with the preferred (2×2) arrangement of Ce^{3+} around the vacancy offers indeed a rationale for the Au pair formation.

However, we point out that the problem is complicated by several reasons. One complication arises because of the calculated, admittedly small energy differences. Francesc Illas and coworkers examined various theoretical models, including the HSE hybrid, to predict the oxidation state of Au adsorbed on the clean $CeO_2(111)$ surface as well as stabilities of the respective adspecies [231]. They concluded that the prediction of the oxidation state is fairly difficult using current DFT-based approaches, since solutions for the minimum energy structures for Au^0 or Au^+ are nearly degenerate in energy. It was found that GGA + U favors $Au^+/CeO_2(111)$ by 0.05 eV. In contrast, HSE predicts $Au^0/CeO_2(111)$ to be 0.15 eV more stable than the positively charged Au causing a Ce^{3+} ion in the surface. This finding is consistent with a recent STM study, which concludes on close-to-neutral charge states for Au atoms adsorbed on defect-poor ceria surfaces [232].

For a ceria surface containing O defects, the complexity of the problem increases drastically and requires to address the influence of the defect concentration. Clearly, a large number of defects in the surface build up considerable amounts of strain due to the high Ce^{3+} concentration. Thus, the thermodynamic driving force to reoxidize some of them to Ce^{4+} is large when Au adatoms offer half-filled 6s orbitals for the redox process [224, 228]. As a consequence, the Au will titrate the Ce^{3+}. The effect of the defect concentration is supported by observation, because the STM revealed that the Au pairs did not homogenously cover the surface, but large variations in the abundance of pairs were observed. This suggests that the local degree of reduction affects the pairs [224]. Definitely, further research is required to get a more comprehensive picture.

4.3 Surface Structure of $V_2O_3(0001)$

Vanadia exists in many different oxide phases, because vanadium can accommodate a large number of oxidation states [233]. The oxidation states relate to varying occupations of the V 3d orbitals. For instance, the oxidation state of vanadium in VO is +2 featuring a (formal) d^3 electron occupation. In V_2O_3, the oxidation state is +3 (d^2), and VO_2 involves V^{+4} (d^1). The highest oxidation state +5 is found in V_2O_5 featuring unoccupied V 3d orbitals.

The d electrons of the vanadium oxides are strongly affected by Coulomb correlation effects [234]. Especially in V_2O_3, correlation steers the subtle balance between localization and delocalization of electrons, giving rise to temperature-dependent metal-to-insulator phase transitions [235]. The latter involve concurrent structural changes. These phase transitions may be also induced by applying hydrostatic pressure [236] or, e.g., doping with Cr [237]. However, the underlying physics of these phase transitions is a much debated issue including surface effects [238, 239].

Concerning catalysis, vanadium oxides are major components of the active phases in many solid oxidation catalysts [180, 240, 241]. Thus, atomic level details of their surface structure is crucial for a rationale of reactivity. For an extensive review on selected case studies of vanadium oxide layers in model catalysis, we refer to [38].

Recent work combining results obtained using *I-V* LEED, atomically resolved STM, grazing angle He scattering, as well as DFT, elucidated the surface structure of $V_2O_3(0001)$ [242]. This surface can be terminated by either one or two V atoms, or an O_3 layer. By virtue of DFT it was shown that surface reconstructions can be thermodynamically more stable than the bulk terminations [243, 244] (cf. Fig. 11). At low oxygen chemical potentials, a vanadyl (V=O) terminated surface was predicted to be the ground state. However, increasing the O chemical potential stabilizes ordered superstructures at $^2/_3$ or $^1/_3$ of full V=O coverage. Even higher chemical potentials of oxygen stabilize a reconstructed O_3 termination. As shown in Fig. 11, in this O_3 termination every other V atom from the second metal layer needs to move up into the first metal layer.

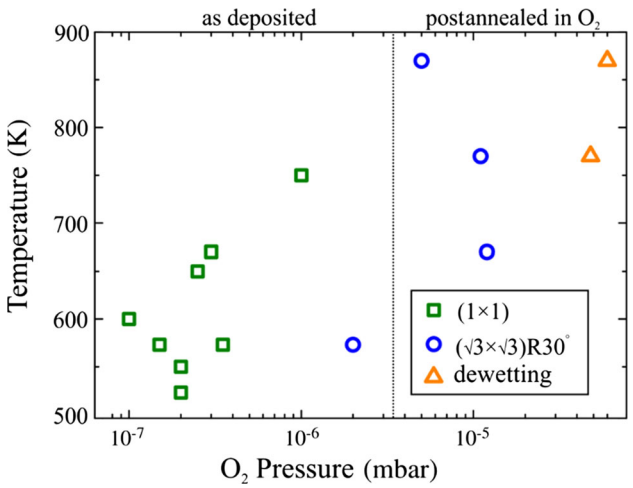

Fig. 12 Experimentally observed surface phases as a function of preparation conditions. Reprinted with permission from [242]. Copyright (2015) American Physical Society

These aforementioned surface phases have been revisited [242, 245]. Fig. 12 shows them as a function of the preparation conditions. For the majority of experiments, a fully V=O covered surface was obtained. However, at higher O_2 pressures and temperatures, the $\left(\sqrt{3}\times\sqrt{3}\right)R30^\circ$ surface, which is partially reconstructed and partially covered by V=O groups, was prepared. Increasing the oxygen partial pressure did not lead to further oxidation, but dewetting or sublimation of the oxide layer was observed instead.

The surface terminations of $V_2O_3(0001)$ were intensively studied using semilocal functionals [243, 244, 246–248]. Recent experimental work [249] supported the O_3 termination invoking arguments based on DFT. Considering the shortcomings of the semilocal approximation, it appears worthwhile to check for robustness of results employing hybrid functionals. As discussed in Sect. 2, the amount of admixed FX is a material-specific quantity and may affect results. Hence, the question arises, whether results critically depend on the mixing ratio a_0 (cf. Eq. 4). We investigated the most important terminations of $V_2O_3(0001)$ using PBE and HSE. In addition to the "as

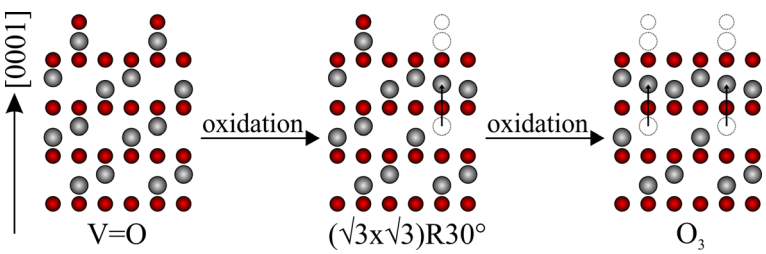

Fig. 11 Structural models of $V_2O_3(0001)$ surface terminations predicted by DFT. V atoms are depicted in *gray*, O atoms are *red*. Reprinted with permission from [242]. Copyright (2015) American Physical Society

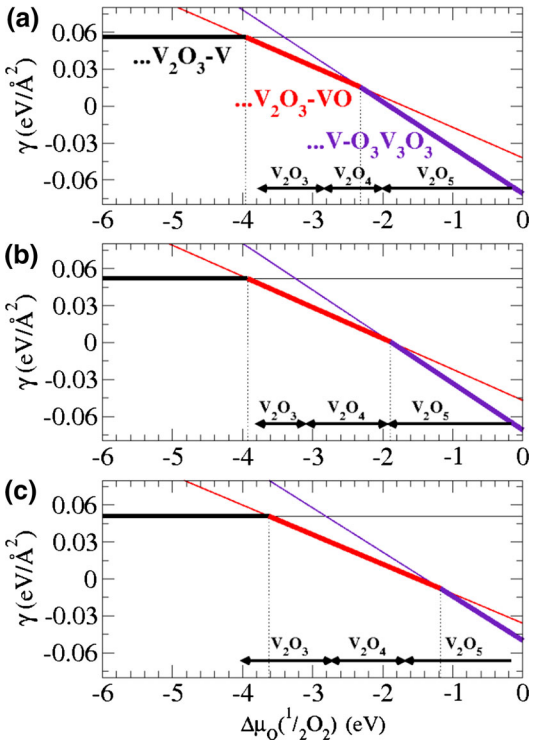

Fig. 13 Surface energy γ as a function of the chemical potential $\Delta\mu_O$ for the most relevant surface terminations obtained using **a** PBE, **b** HSE(10 % FX), and **c** HSE (25 % FX). Reprinted with permission from [242]. Copyright (2015) American Physical Society

defined" value $a_0 = 0.25$, we also used $a_0 = 0.10$, which was recently suggested for VO_2 [250].

The calculated phase diagrams obtained with PBE and HSE ($a_0 = 0.1$ and 0.25) are presented in Fig. 13. The black arrows at the bottom refer to the stable bulk phases at respective chemical potentials of oxygen. Our PBE results agree excellently with previously published results of Georg Kresse and coworkers obtained using the PW91 GGA functional [243]. PBE and PW91 [251, 252] are closely related in terms of their analytical forms. Hence, the agreement does not come as a surprise. Concerning HSE results, increasing a_0 shifts the boundary for the equilibrium between V = O and O_3 terminations towards more positive potentials, i.e. towards higher oxygen pressures for a given temperature. HSE ($a_0 = 0.25$) predicts a value for the phase equilibrium of −1.1 eV corresponding to—at 900 K—an oxygen pressure of about 1 mbar.

We do not claim that a simple hybrid functional like HSE describes the aforementioned Coulomb correlation effects in V_2O_3 correctly. Neither should the aforementioned results be interpreted quantitatively. Nonetheless, we believe that the PBE and the closely related PW91 functional overemphasize phase stability of the O_3 termination under reducing conditions, i.e. at low chemical potentials of oxygen. Note that the hybrid functionals only marginally modify the stability range for the bulk phase of V_2O_5 relative to PBE results. We learn from the phase diagram, that the O_3 termination is competing with the bulk phase of V_2O_5. This agrees with the observation, which indicates sublimation of the oxide layer (cf. Fig. 12).

Reliability of HSE for the vanadium sesquioxide is supported by theoretical work of Angel Rubio and coworkers [253]. They showed that HSE performs well for the paramagnetic phase of bulk V_2O_3. Our own work showed, that HSE outperforms PBE in terms of enthalpies of formation for the bulk phases of V_2O_3, V_2O_4, as well as V_2O_5 [242]. HSE results agree better with observed values (cf. Supporting Information of [242]).

In conclusion, HSE predicts the V=O termination to be stable under relevant experimental conditions and destabilizes the O_3 termination relative to the V_2O_5 bulk phase in agreement with observation. Conceding errors in the chemical potential of oxygen obtained, which may be as large as several hundred meV, translates to several orders of magnitude of an error in the pressure. Even within these uncertainties, the phase equilibrium between V=O and O_3 cannot be shifted in favor of the O_3 termination, i.e. the conditions cannot be reached experimentally. This result is in contrast to findings of previous studies [243, 244], which we attribute to the right balance between nonlocal and semilocal information contained in the HSE hybrid functional.

4.4 Adsorption of Water on the Fe_3O_4(111) Surface

Iron oxides represent an important class of materials, because of their widespread technical applications [254]. In catalysis, hematite (Fe_2O_3) and magnetite (Fe_3O_4), are used in the preparation of the iron catalyst employed in the Haber–Bosch process, i.e. the synthesis of NH_3 from N_2 and H_2 [233, 255]. Hematite is the most stable iron oxide phase under ambient conditions, however under more reducing conditions, i.e. high temperatures and low oxygen partial pressures, magnetite becomes the prevalent phase [256, 257].

At temperatures greater than the so-called Verwey transition temperature of *ca.* 122 K, magnetite crystallizes in a cubic, inverse spinel structure [234]. This means that tetrahedral (A) sites are occupied by Fe^{3+} (high-spin d^5) and octahedral (B) sites are occupied by 50 % of Fe^{2+} (high-spin d^6) and 50 % of Fe^{3+}, which are randomly distributed. It is a ferrimagnet, i.e. spins located at tetrahedral and octahedral iron sites are antiferromagnetically coupled. These local magnetic moments do not compensate each other, leading to a net magnetic moment of about 4 μ_B per Fe_3O_4 formula unit [258].

The predominant natural growth facet of magnetite is a surface in (111) orientation [259]. Hence, the (111) surface is relevant for studying ambient conditions.

We examined the adsorption of water at the $Fe_3O_4(111)$ surface using PBE + U(3.8) and the HSE hybrid to test for robustness of PBE + U results [260]. HSE is corrected for dispersion-type van der Waals interactions by a c_6/r^6 term as introduced by Stefan Grimme [198, 199, 261]. As discussed in [262], it is mandatory to use a sufficient number of layers in the slab model, because 3d electrons localize in subsurface iron layers upon ionic relaxation, which in turn incurs Jahn–Teller-type distortions. This effect is known as orbital or charge ordering [263, 264] and lowers the energy of the slab. To accommodate these aforementioned relaxation effects, the models used in [260] employ 12 atomic layers (cf. Fig. 14).

Table 3 presents local magnetic moments for the surface Fe ions obtained using PBE + U(3.8) and HSE + D, respectively. PBE + U values compare well with results given in [262]. Local magnetic moments of the octahedrally and tetrahedrally coordinated Fe ions in the bulk amount to 3.9 and −4.1 μ_B, respectively. Smaller magnetic moments in surface ions indicate additional electron localization, i.e. a reduction of surface iron ions. HSE + D and PBE + U(3.8) results are de facto identical.

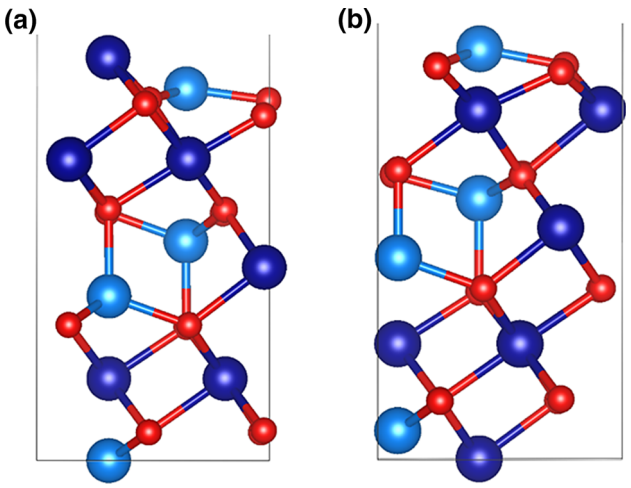

Fig. 14 Relaxed slab models for **a** Fe_{oct2} and **b** Fe_{tet1} terminated $Fe_3O_4(111)$ surfaces. Octahedrally and tetrahedrally coordinated Fe ions are shown in *dark* and *light blue*, respectively. Reprinted with permission from [260]. Copyright (2016) American Chemical Society

Table 3 Local magnetic moments (μ_B) of surface iron ions in the Fe_{oct2} and Fe_{tet1} terminated $Fe_3O_4(111)$ surfaces obtained using PBE + U(3.8) and HSE + D

Termination	Fe-oct2		Fe-tet1
Surface ions	Fe_{oct}	Fe_{tet}	Fe_{tet}
PBE + U(3.8)[a]	3.58	−3.58	−3.51
PBE + U(3.8)	3.54	−3.56	−3.51
HSE + D	3.52	−3.56	−3.51

[a] Ref. [262]

From a practitioner's point of view, DFT + U suffers from many local minima on the corresponding potential energy surface. This hampers the determination of the electronic as well as magnetic ground state of Fe_3O_4. For example, after adsorption of an H_2O molecule on the $Fe_3O_4(111)$ surface, the spin density or local magnetic moments per surface iron ion will be modified with respect to the clean surface. The precise value cannot be known a priori. Starting the HSE structure optimization on top of PBE + U(3.8) structures yields identical local magnetic moments and spin-orders as found by using the PBE + U(3.8) approach. This protocol turned out to be very robust and is suitable to confirm electronic and magnetic ground states of the hydrated surfaces. It appears that the problem of metastable minima plaguing the DFT + U approach is largely bypassed using a hybrid functional like HSE. This tremendously facilitates calculations.

Water adsorbed on the $Fe_3O_4(111)$ surface has been recently studied combining single crystal adsorption calorimetry (SCAC), infra-red spectroscopy, and DFT [265]. As shown in Fig. 15, the initial adsorption energy of water at temperatures greater than 120 K amounts to 100 kJ/mol. Figure 16a shows two IR bands at 2720 and 2695 cm^{-1} using D_2O adsorbed on $Fe_3O_4(111)$. These two bands are shifted by 18 and 16 cm^{-1}, respectively, when ^{18}O labeled water was dosed. Preparing the surface using ^{18}O and dosing $D_2^{16}O$ does not incur such an isotope shift. Thus, the observed OD stretching modes cannot involve O atoms originating from the surface.

Figure 16b shows that the modes involved in the two bands are coupled and cannot stem from spatially separated, individual OD groups. Dosing light water, the

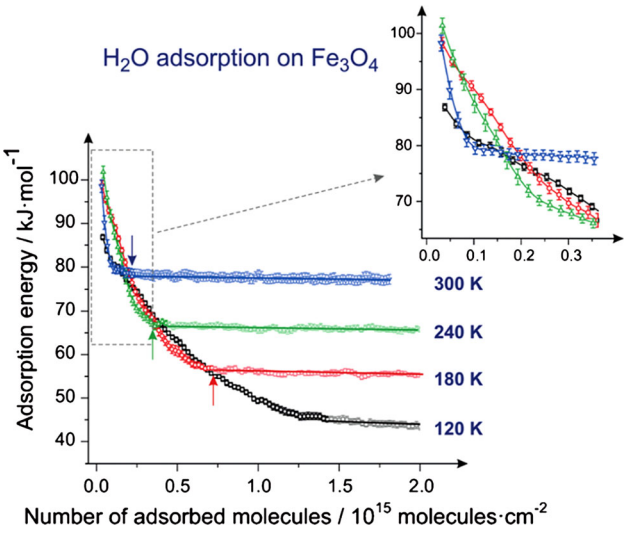

Fig. 15 Adsorption energies of H_2O on $Fe_3O_4(111)$ at different temperatures based on molecular beam techniques. Reprinted and adapted with permission from [265]. Copyright (2015) John Wiley and Sons

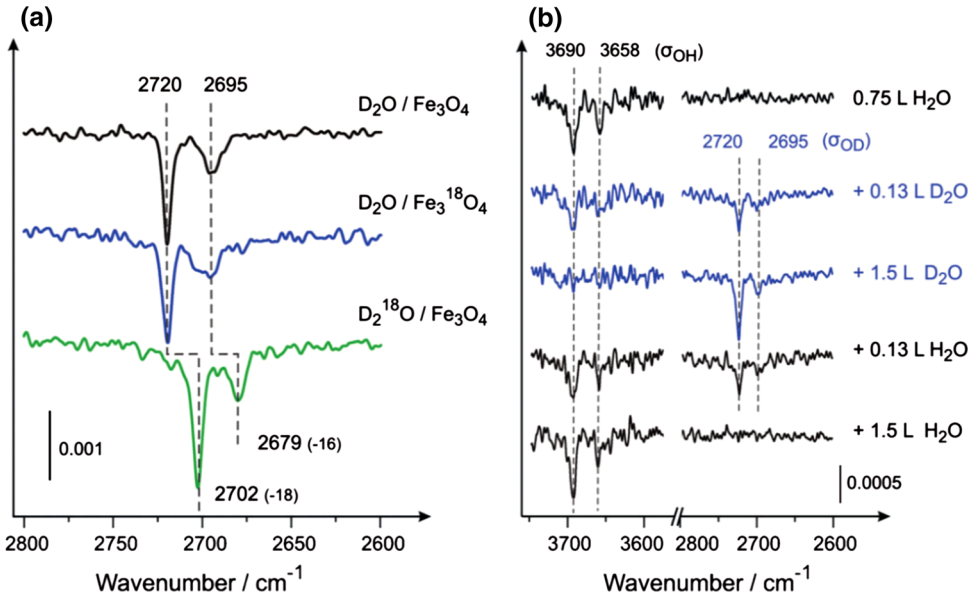

Fig. 16 **a** IR spectra for D_2O and $D_2^{18}O$ adsorbed on the $Fe_3O_4(111)$ surfaces prepared using ^{16}O and ^{18}O at a temperature of 300 K. **b** Series of IR spectra recorded at 300 K, when H_2O was reversibly replaced by D_2O. Reprinted with permission from [265]. Copyright (2015) John Wiley and Sons

respective wavenumbers amount to 3690 and 3658 cm^{-1}, typical of OH stretching modes. Exposing the surface to some D_2O results in decreased peak intensities and two bands at 2720 and 2695 cm^{-1} appear. Upon further exposure to D_2O, the two peaks at around 3700 cm^{-1} disappear and the two corresponding signals at 2700 cm^{-1} appear with the same characteristic time constant. Hence, these IR signals originate from coupled modes.

Several minimum energy adsorption structures for one, two, and three water molecules at the $Fe_3O_4(111)$ surface were calculated using PBE + U(3.8) [260]. As discussed above, a single water molecule dissociatively adsorbed at the surface is not reconcilable with observed isotopic shifts. This is because of the formation of a surface OH group in case of dissociative adsorption, which would inevitably lead to a shift in one of the IR bands upon isotopic labeling of the surface. In case of molecular adsorption of water, one of the two (calculated) wavenumbers is substantially red-shifted and as a consequence their difference is much larger than the experimentally observed difference in bands (25 cm^{-1}, see also Fig. 8b in [260]).

Based on calculated adsorption energies and IR wavenumbers (including isotope shifts), only a water dimer-type species, involving a dissociated and an intact water molecule at the Fe_{oct2} terminated $Fe_3O_4(111)$ surface, is reconcilable with experiment. The average PBE + U(3.8) adsorption enthalpy for this water dimer amounts to 109 kJ/mol, which agrees excellently with the observed value (100 kJ/mol; cf. Figure 15). Unscaled IR wavenumbers obtained using PBE + U(3.8) for the so-called terminal OD stretching modes of this adsorption complex amount to 2758 and 2728 cm^{-1}. Scaling of the wavenumbers with factors, that are either taken from the literature [266] or derived from the 'experiment/theory' ratio of respective averages between symmetric and antisymmetric stretching modes of molecular water [265, 267], leads to a 1 % decrease of PBE wavenumbers. Scaled wavenumbers agree better with observation. Similar successful scaling was applied to the stretching modes of terminal or "free" OH groups (cf. [34]) of hydroxylated silica surfaces using the B3LYP hybrid functional [268, 269].

5 Summary, Limitations, and Future Prospects

5.1 Summary

We learn from the case studies discussed in this work as well as from the work published in the literature, that hybrid functionals applied to semiconducting and insulating metal oxides outperform semilocal functionals in terms of (i) band gaps [128, 161, 270, 271], (ii) oxygen defect formation energies [230, 272], and (iii) activation barriers [97, 190, 197, 273]. Previously stated by Gianfranco Pacchioni, these improvements are closely connected to decreased SIEs and thereby enhanced charge as well as spin localization [28]. The admixture of non-local FX to semilocal exchange is beneficial for the "stretched-bond" situation in transition structures [60]. A quarter or 25 % of FX complemented by 75 % of semilocal exchange proved a good average for molecules (including transition metal oxides [274]) and semiconductors [270]. Metallic systems need less or no FX [77, 128]. A screened FX interaction, effective at shorter interelectron distances like in the HSE hybrid, yields very accurate 'medium sized' band gaps of (simple) semiconductors [275]. For other properties like magnetic exchange

couplings, FX effective on the long-range part of the Coulomb interaction was shown to yield more accurate results [276]. Details on magnetic properties obtained with hybrid functionals applied to extended systems can be found in the excellent review by Jean Paul Malrieu [277] or Francesc Illas [278]. Based on our practical experience, potential energy surfaces of hybrid functionals feature substantially fewer meta-stable local minima as encountered in DFT + U calculations. Thus, the likelihood of getting trapped in spurious minima in the course of electronic optimizations is substantially smaller. This enhances computational efficiency of calculations on magnetic systems like the magnetite surfaces discussed in Sect. 5 [260, 265]. Good performance of the B3PW91 hybrid functional applied to iron oxide has been reported in [279].

Oxygen defect formation energies are important descriptors to assess reactivity of oxidation catalysts [42]. Ceria is a reducible oxide with outstanding catalytic properties, because of its high reducibility [212, 280]. Accurate measurements of the O defect formation energy in ceria surfaces under well-defined conditions is difficult [281–283]. However, an estimate of 4.2 ± 0.3 eV corrected for the electron-hopping barrier was provided [29]. The error bar of 0.3 eV was estimated, and it may be even larger due to the reasons given in [29]. PBE + U using conventional values for U ranging between 4 and 6 eV [284] underestimates O vacancy formation energies by *ca.* 1.5 eV. A hybrid functional like HSE improves O vacancy formation energies significantly and underestimates them by *ca.* 0.8 eV.

Defects are commonly entangled with polaron formation. Hence, stabilization of the system by lattice distortions or relaxations plays a crucial role [285–287]. Consequently, high accuracy in lattice parameters as well as elastic constants is important for metal oxides [197]. For semiconductors and insulators in general and ceria in particular, the HSE or PBE0 hybrids perform with high accuracy [77, 175]. Results obtained using the B3LYP hybrid functional are slightly more off [123, 288]. Hybrid functionals benefit from the possibility to consistently optimize cells and atomic positions, because of available gradients and stress tensors (see, e.g., [30, 289, 290]) at affordable computational cost. Accomplishing hybrid functional calculations is the best a DFT practitioner can currently do, when dealing with insulating oxides like ceria, based on the fact that relaxation of atoms and cells can be *consistently* carried out.

5.2 Limitations

Global as well as range-separated hybrids run into problems, when applied to metallic systems [77, 128, 129]. The situation is particularly bad for transition metals, such as Fe or Cr, featuring so-called itinerant magnetism [65, 77, 291]. Ref. [291] reports, that HSE for Cr using the antiferromagnetically ordered state (cf. [292]) yields the lowest energy structure, however the equilibrium lattice constant is overestimated by 23 %. Similar findings are reported for the complex structure of Mn [291, 293]. The problem for these transition metals arises from overly localized orbitals using a hybrid functional. The metal is erroneously described as a so-called Hund's rule magnet featuring spatially too localized moments. This has been shown by the overestimated local magnetic moment of Fe compared to (e.g.) PBE results [77]. It appears plausible that for these systems the combination of non-local FX and semilocal correlation is unbalanced, and non-local correlation (e.g. based on the generalized RPA) is required. RPA lattice parameters for Fe, Co, and Ni were reported to be in good agreement with experiment [294].

Peter Feibelman's CO/Pt(111) puzzle offers another cautionary moment [295]. This problem deals with the preferred adsorption site of CO on the close packed Pt(111) surface, i.e., atop versus hollow positions, and the conflict between experiment and DFT results obtained with semilocal approximations. As described in [130, 296], hybrid functionals like HSE overestimate band widths of the d states in metallic surfaces, which results in adverse effects concerning the binding of CO, although the HOMO–LUMO gap in CO is properly described. The importance of the gap for CO adsorption on transition metals was shown in [297]. The adsorption energy differences for top and hollow sites amount to *ca.* 0.1 eV, which is a small value. Thus, the problem represents a veritable challenge for the computational modelling. Sure enough, the proper description of the electronic structure is important, but only one aspect of the entire problem. For instance, thermal effects may also play a role with regard to the aforementioned narrow energy range of 0.1 eV. We agree with the conclusions drawn in [298]. Whenever small energy differences or near-degeneracies require an evaluation or assessment, also other properties than mere energies need to be considered in order to provide a bigger picture.

Concerning CO adsorption, it appears that non-local correlation effects corresponding to dispersion-type van der Waals interactions are the clue underlying site preferences of CO on Pt(111) [95, 299, 300]. Additionally, the preference of CO to adsorb in atop position, e.g., on the Cu(111) surface was found using embedded, correlated wavefunction-based methods like configuration interaction [301], but also with a kinetic energy density functional approach [302].

Straightforward application of hybrids to the so-called strongly correlated vanadium oxides VO_2 and V_2O_3 may be problematic. These systems involve d states drastically changing character from rather band-like (delocalized) to atom-like (localized) depending on the crystal structure. The involved Coulomb correlation effects among electrons

are difficult to describe accurately within KS-DFT [37, 303, 304]. A profound discussion of a state-of-the-art description of the electronic properties of vanadium oxides is beyond the scope of the present work. We refer to the review article of Karsten Held and coworkers and therein cited references instead [305].

Recent computational studies applied hybrid functionals like HSE to VO_2 [163, 242, 250, 253, 306, 307]. While the situation is not that bad for paramagnetic V_2O_3 [163, 253], earlier HSE calculations using the "as defined" 25 % of FX, predicted a band gap for the metallic rutile VO_2 phase and magnetic ground states for both monoclinic and rutile phases, which are not observed [307]. Recent fixed-node diffusion quantum Monte Carlo (FN-DMC) results for VO_2 indicate that the ground state is spin polarized, because ferromagnetically and antiferromagnetically ordered spins provide lower total energies than the corresponding unpolarized result [308]. It is noteworthy that the FN-DMC uses PBE0 trial wavefunctions employing various FX admixing factors. Recently, it was shown that decreasing the amount of admixed FX to 10 % qualitatively improves HSE results for the VO_2 phases [250]. Similar problems have been reported for MnO phases [309].

The inevitable parameters used in a hybrid functional, such as the amount of FX and possible screening parameters, were shown to be material-specific (e.g. [76], [310], [271], [78], [311], [312]). The admixing ratio of FX can be physically motivated, because the generalized KS potential mimics the self-energy as amply discussed in [141]. Employing "dielectric adaptation of FX" or equivalently "statically screened exchange" (cf. [75], [313–315]), a series of successful calculations on complex semiconducting and insulating metal oxides like ZnO or TiO_2, but also on organic–inorganic perovskites like $CH_3NH_3PbI_3$ [316], could be accomplished. We emphasize that this adaptation is more than a mere fitting, it takes care of dielectric screening or equivalently some of the electron correlation effects. In light of the successes reported in the literature, potential limitations of hybrids incurred by a fixed amount of FX, which would naturally restrict their universal application, appear remediable though.

From a practitioner's point of view, the computational workload imposed by hybrid functionals is considerably larger compared with semilocal functionals. For instance, determining a transition structure for chemical reactions on surfaces is a non-trivial task involving high computational cost [190, 197]. Nonetheless, it is necessary to provide these benchmark results, not only for the sake of theory, but also to have reference values at hand, which can be compared with state-of-the-art experimental results. At the moment, the computational workload prevents, e.g., industrial research in catalysis relying on a screening of several thousand materials in short amount of time. With regard to academic research, hybrid functionals represent an important alternative to semilocal approximations, whenever there is need for results obtained with higher rung functionals of supposed higher accuracy. Standard optimizations are certainly feasible by nowadays technologies, either relying on in-house clusters of academic institutions or high-performance computer centers. Developments exploiting non-conventional computer architecture like graphical processing units (GPUs) promise to drastically enhance times spent to compute the FX energy [317] required for hybrid functionals. Additionally, software developments in terms of better exploitation of available high-performance resources is certainly prerequisite to efficient simulations on extended systems [318], particularly so for dynamics simulations [159, 319].

5.3 Prospects

Hybrid functionals have become a standard tool in computational catalysis or materials science and will enjoy widespread applications in the future. However, they do not represent a panacea in light of above mentioned shortcomings. This invites the question, how to do it better. If one adheres to DFT, developments in functionals of the fifth rung on Jacob's ladder, i.e. fully non-local hybrid functionals involving orbital dependence in the correlation energy, appears to be the logical step. Currently, RPA-based functionals are an active field of research (cf. [87] and therein cited references). It is expected that fifth rung functionals will overcome the limitations of conventional hybrid functionals. However, the generalized RPA involves an even higher computational workload, because it bears resemblance to wavefunction-based methods [86, 320, 321]. Developments with respect to computer hardware as well as algorithms used in the software will improve the situation (e.g. [106], [322], [323]). Related to extended systems, RPA-based functionals are not available self-consistently, i.e. orbitals and orbital energies need to be generated in a first step. KS-orbitals are conventionally used for that purpose. However, if semilocal approximations fail, e.g., to describe the band gap accurately, orbitals obtained using hybrid functionals represent a viable option (cf., e.g., [324, 325]).

Currently, there is a revived interest in embedding techniques (e.g., [326–333]). In order to save computing time, hybrids could be employed within an embedded framework, representing the so-called "high-level method". Alternatively, when doubts arise on the accuracy of the hybrid functional used, they could be employed to describe the "low-level domain", and more accurate generalized RPA or post-HF wavefunction-based methods can be used instead. Embedding hybrid functionals is certainly a way to render calculations more efficient. However,

technically this is not a trivial task, justifying the many promising research activities [334–337].

6 Final Remarks

A recent article by Axel Becke [338] nicely reviews the past fifty years of developments in DFT. It concludes with the interesting question, whether the efforts in making functionals more accurate will continue to satisfy DFT users in terms of speed. Semilocal functionals will remain a significant tool in computational chemistry and physics, because of the speed argument. Hybrid functionals represent an important step partially merging wavefunction-based theory (HF) with DFT (and vice versa). The additional non-local information originating from the one-electron density matrix required to compute the FX energy can substantially improve upon semilocal results for band gaps, defect formation energies, and activation barriers, but currently not for relatively low computational cost. *There ain't no such thing as a free lunch.*

If we want to compare computational results with observation, we need structural models to guarantee a well-defined scenario for both, experiment and theory [39]. For such an endeavor, we have to keep in mind merits and limits of the approximations involved in DFT, as well as of pros and cons of underlying structural models used in actual calculations. Hybrid functionals relying on a minimal number of physically motivated parameters represent a very useful rung on Jacob's ladder. Within their admitted limits, they offer a valuable way to check semilocal results including DFT + U. However, successful research in catalysis and materials science will continue to be pillared by DFT, wavefunction theory,[1] as well as state-of-the-art experiments employing several, possibly complementary techniques.

Acknowledgments I am indebted to Prof. Joachim Sauer for his continuous support and for many insightful discussions. I gratefully thank my ambitious coworkers Christopher Penschke, Thomas Kropp, and Xiaoke Li. I especially thank Thomas and Christopher for proofreading parts of the manuscript. I sincerely acknowledge the numerous fruitful collaborations and discussions with Prof. Hajo Freund (Fritz-Haber-Institut der Max-Planck-Gesellschaft), Prof. Niklas Nilius (Carl von Ossietzky Universität Oldenburg), and Prof. Swetlana Schauermann (Christian-Albrechts-Universität zu Kiel). These collaborative efforts generated decisive results, which form the basis for many conclusions drawn in this perspective article. I thank Prof. Christof Wöll (Karlsruher Institut für Technologie), Dr. M. Verónica Ganduglia-Pirovano (Instituto de Catálisis y Petroleoquìmica), Dr. Helmut Kuhlenbeck, and Dr. Shamil Shakhutdinov (Fritz-Haber-Institut der Max-Planck-Gesellschaft) for many fruitful and stimulating discussions. Several generous grants for computing time at the HLRN (North-German Supercomputing Alliance in Berlin and Hannover) and JUROPA (Forschungszentrum Jülich) are thankfully acknowledged. I owe tremendous thanks to Dr. Jens Döbler, Dr. Christian Tuma, and Dr. Stefan Wollny, representatives of the HLRN, for their continuous efforts. Financial support by the Deutsche Forschungsgemeinschaft within the Sonderforschungsbereich (SFB) 1109, the COST action CM1104, the Fonds der Chemischen Industrie (FCI), and the Stiftung Industrieforschung, Humboldt-Universität zu Berlin, are gratefully acknowledged.

[1] The term "wavefunction theory" is supposed to comprise higher-order density-matrix formalisms, Green function approaches, and Quantum Monte Carlo techniques, in addition to methods conventionally used in quantum chemistry (perturbation theory, configuration interaction, coupled-cluster).

References

1. Kohn W, Sham LJ (1965) Phys Rev 140:1133
2. Dreizler RM, Gross EKU (1990) Density functional theory. Springer, Berlin
3. Jones RO, Gunnarsson O (1989) Rev Mod Phys 61:689
4. Grabowski B, Wippermann S, Glensk A, Hickel T, Neugebauer J (2015) Phys Rev B 91:201103
5. Thiel W (2014) Angew Chem Int Ed 53:8605
6. Curtiss LA, Raghavachari K, Redfern PC, Pople JA (1997) J Chem Phys 106:1063
7. Zhao Y, Truhlar DG (2005) J Phys Chem A 109:5656
8. Csonka GI, Perdew JP, Ruzsinszky A, Philipsen PHT, Lebegue S, Paier J, Vydrov OA, Ángyán JG (2009) Phys Rev B 79:155107
9. Rapps T, Ahlrichs R, Waldt E, Kappes MM, Schooss D (2013) Angew Chem Int Ed 52:6102
10. Koch W, Holthausen MC (2001) A chemist's guide to density functional theory. Wiley-VCH Verlag GmbH, Weinheim
11. Ozolins V, Körling M (1993) Phys Rev B 48:18304
12. Peverati R, Truhlar DG (2012) J Chem Theory Comput 8:2310
13. Kim Y-S, Marsman M, Kresse G, Tran F, Blaha P (2010) Phys Rev B 82:205212
14. Payne MC, Teter MP, Allan DC, Arias TA, Joannopoulos JD (1992) Rev Mod Phys 64:1045
15. Goedecker S (1999) Rev Mod Phys 71:1085
16. Jensen F (2002) J Chem Phys 116:7372
17. Furche F (2001) Phys Rev B 64:195120
18. Sauer J (1989) Chem Rev 89:199
19. Pacchioni G, Lomas JR, Illas F (1997) J Mol Catal A: Chem 119:263
20. Gillan MJ (1997) Contemp Phys 38:115
21. Pykavy M, Stämmler V, Seiferth O, Freund HJ (2001) Surf Sci 479:11
22. Schmitt I, Fink K, Stämmler V (2009) Phys Chem Chem Phys 11:11196
23. Müller C, Hermansson K, Paulus B (2009) Chem Phys 362:91
24. Perdew JP, Zunger A (1981) Phys Rev B 23:5048
25. Ruzsinszky A, Perdew JP, Csonka GI, Vydrov OA, Scuseria GE (2007) J Chem Phys 126:104102
26. Janesko BG, Henderson TM, Scuseria GE (2009) Phys Chem Chem Phys 11:443
27. Ganduglia-Pirovano V, Hofmann A, Sauer J (2007) Surf Sci Rep 62:219
28. Pacchioni G (2008) J Chem Phys 128:182505
29. Paier J, Penschke C, Sauer J (2013) Chem Rev 113:3949
30. Freysoldt C, Grabowski B, Hickel T, Neugebauer J, Kresse G, Janotti A, Van de Walle CG (2014) Rev Mod Phys 86:253
31. Zhao Y, Gonzalez-Garcia N, Truhlar DG (2005) J Phys Chem A 109:2012
32. Janesko BG, Scuseria GE (2008) J Chem Phys 128:244112

33. Kohn W, Meir Y, Makarov DE (1998) Phys Rev Lett 80:4153
34. Sauer J, Ugliengo P, Garrone E, Saunders VR (1994) Chem Rev 94:2095
35. Kümmel S, Kronik L (2008) Rev Mod Phys 80:3
36. Cohen AJ, Mori-Sanchez P, Yang W (2012) Chem Rev 112:289
37. Perdew JP, Ruzsinszky A, Constantin LA, Sun J, Csonka GI (2009) J Chem Theory Comput 5:902
38. Kuhlenbeck H, Shaikhutdinov S, Freund H-J (2013) Chem Rev 113:3986
39. Sauer J, Freund H-J (2015) Catal Lett 145:109
40. Jacob D, Haule K, Kotliar G (2008) EPL 84:57009
41. Mars P, van Krevelen DW (1954) Chem Eng Sci 3(Supplement 1):41
42. Sauer J, Döbler J (2004) Dalton Trans 19:3116
43. Keating PRL, Scanlon DO, Morgan BJ, Galea NM, Watson GW (2012) J Phys Chem C 116:2443
44. Pacchioni G, Freund H (2013) Chem Rev 113:4035
45. Solans-Monfort X, Branchadell V, Sodupe M, Sierka M, Sauer J (2004) J Chem Phys 121:6034
46. Nolan M (2010) Chem Phys Lett 499:126
47. Kropp T, Paier J (2015) J Phys Chem C 119:23021
48. Gillan MJ, Alfè D, De Gironcoli S, Manby FR (2008) J Comput Chem 29:2098
49. Pisani C, Maschio L, Casassa S, Halo M, Schütz M, Usvyat D (2008) J Comput Chem 29:2113
50. Nolan SJ, Gillan MJ, Alfè D, Allan NL, Manby FR (2009) Phys Rev B 80:165109
51. Paier J, Diaconu CV, Scuseria GE, Guidon M, VandeVondele J, Hutter J (2009) Phys Rev B 80:174114
52. Binnie SJ, Nolan SJ, Drummond ND, Alfè D, Allan NL, Manby FR, Gillan MJ (2010) Phys Rev B 82:165431
53. Voloshina E, Usvyat D, Schütz M, Dedkov Y, Paulus B (2011) Phys Chem Chem Phys 13:12041
54. Pisani C, Schütz M, Casassa S, Usvyat D, Maschio L, Lorenz M, Erba A (2012) Phys Chem Chem Phys 14:7615
55. Booth GH, Grüneis A, Kresse G, Alavi A (2013) Nature 493:365
56. Grüneis A (2015) J Chem Phys 143:102817
57. Grüneis A (2015) Phys Rev Lett 115:066402
58. Perdew JP, Schmidt K (2001) In: Van Doren VE, Van Alsenoy K, Geerlings P (eds) Density-functional theory and its applications to materials. American Institute of Physics, Melville
59. Perdew JP (2013) MRS Bull 38:743
60. Perdew JP, Staroverov VN, Tao J, Scuseria GE (2008) Phys Rev A 78:052513
61. Perdew JP, Kurth S, Zupan A, Blaha P (1999) Phys Rev Lett 82:2544; Erratum: (1999) ibid 82:5179
62. De Jong GT, Geerke DP, Diefenbach A, Sola M, Bickelhaupt FM (2005) J Comput Chem 26:1006
63. Sun J, Marsman M, Csonka GI, Ruzsinszky A, Hao P, Kim Y-S, Kresse G, Perdew JP (2011) Phys Rev B 84:035117
64. Sun J, Marsman M, Ruzsinszky A, Kresse G, Perdew JP (2011) Phys Rev B 83:121410
65. Janthon P, Luo SJ, Kozlov SM, Vines F, Limtrakul J, Truhlar DG, Illas F (2014) J Chem Theory Comput 10:3832
66. Maier TM, Boese AD, Sauer J, Wende T, Fagiani M, Asmis KR (2014) J Chem Phys 140:204315
67. Vosko SH, Wilk L, Nusair M (1980) Can J Phys 58:1200
68. Becke AD (1986) J Chem Phys 84:4524
69. Perdew JP, Wang Y (1992) Phys Rev B 45:13244
70. Perdew JP, Burke K, Ernzerhof M (1996) Phys Rev Lett 77:3865; Erratum: (1997) ibid 78:1396
71. Armiento R, Mattsson AE (2005) Phys Rev B 72:085108
72. Mattsson AE, Armiento R (2009) Phys Rev B 79:155101
73. Tao JM, Perdew JP, Staroverov VN, Scuseria GE (2003) Phys Rev Lett 91:146401
74. Perdew JP, Constantin LA (2007) Phys Rev B 75:155109
75. Seidl A, Görling A, Vogl P, Majewski JA, Levy M (1996) Phys Rev B 53:3764
76. Asmis KR, Santambrogio G, Brümmer M, Sauer J (2005) Angew Chem Int Ed 44:3122
77. Paier J, Marsman M, Hummer K, Kresse G, Gerber IC, Ángyán JG (2006) J Chem Phys 124:154709; Erratum: (2006) ibid 125:249901
78. Ramprasad R, Zhu H, Rinke P, Scheffler M (2012) Phys Rev Lett 108:066404
79. Perdew JP, Emzerhof M, Burke K (1996) J Chem Phys 105:9982
80. Zhao Y, Truhlar DG (2006) J Phys Chem A 110:13126
81. Zhao Y, Truhlar DG (2008) Theor Chem Acc 120:215
82. Jaramillo J, Scuseria GE, Ernzerhof M (2003) J Chem Phys 118:1068
83. Arbuznikov AV, Kaupp M (2007) Chem Phys Lett 440:160
84. Haunschild R, Janesko BG, Scuseria GE (2009) J Chem Phys 131:154112
85. Kurth S, Perdew JP (1999) Phys Rev B 59:10461; Erratum: (1999) ibid 60:11212
86. Grüneis A, Marsman M, Harl J, Schimka L, Kresse G (2009) J. Chem. Phys. 131:154115
87. Ren X, Rinke P, Joas C, Scheffler M (2012) J Mater Sci 47:7447
88. Zhao Y, Lynch BJ, Truhlar DG (2004) J Phys Chem A 108:4786
89. Schwabe T, Grimme S (2006) Phys Chem Chem Phys 8:4398
90. Karton A, Tarnopolsky A, Lamere J-F, Schatz GC, Martin JML (2008) J Phys Chem A 112:12868
91. Harris FE, Monkhorst HJ, Freeman DL (1992) Algebraic and diagrammatic methods in Many–Fermion theory. Oxford University Press, New York
92. Niquet YM, Fuchs M, Gonze X (2003) Phys Rev A 68:032507
93. Dobson JF, Gould T (2012) J Phys: Condens Matter 24:073201
94. Harl J, Kresse G (2008) Phys Rev B 77:045136
95. Ren X, Rinke P, Scheffler M (2009) Phys Rev B 80:045402
96. Ma J, Michaelides A, Alfè D, Schimka L, Kresse G, Wang E (2011) Phys Rev B 84:033402
97. Karlicky F, Lazar P, Dubecky M, Otyepka M (2013) J Chem Theory Comput 9:3670
98. Macher M, Klimes J, Franchini C, Kresse G (2014) J Chem Phys 140:084502
99. Bao JL, Yu HS, Duanmu K, Makeev MA, Xu X, Truhlar DG (2015) ACS Catal 5:2070
100. Ren X, Tkatchenko A, Rinke P, Scheffler M (2011) Phys Rev Lett 106:153003
101. Paier J, Ren X, Rinke P, Scuseria GE, Grüneis A, Kresse G, Scheffler M (2012) New J Phys 14:043002
102. Hellgren M, Rohr DR, Gross EKU (2012) J Chem Phys 136:034106
103. Jemai M, Delion DS, Schuck P (2013) Phys Rev C 88:044004
104. Bleiziffer P, Hesselmann A, Görling A (2013) J Chem Phys 139:084113
105. Ngoc Linh N, Colonna N, de Gironcoli S (2014) Phys Rev B 90:045138
106. Moussa JE (2014) J Chem Phys 140:014107
107. Hellgren M, Caruso F, Rohr DR, Ren X, Rubio A, Scheffler M, Rinke P (2015) Phys Rev B 91:165110
108. Bleiziffer P, Krug M, Görling A (2015) J Chem Phys 142:244108
109. Becke AD (1993) J Chem Phys 98:1372
110. Harris J, Jones RO (1974) J Phys F: Met Phys 4:1170
111. Langreth DC, Perdew JP (1977) Phys Rev B 15:2884
112. Dirac PAM (1929) Proc R Soc Lond A 123:714
113. Slater JC (1951) Phys Rev 81:385
114. Becke AD (1993) J Chem Phys 98:5648
115. Becke AD (1988) Phys Rev A 38:3098

116. Perdew JP (1991) In: Ziesche P, Eschrig H (eds) Electronic structure of solids. Akademie, Berlin
117. Lee CT, Yang WT, Parr RG (1988) Phys Rev B 37:785
118. Miehlich B, Savin A, Stoll H, Preuss H (1989) Chem Phys Lett 157:200
119. Stephens PJ, Devlin FJ, Chabalowski CF, Frisch MJ (1994) J Phys Chem 98:11623
120. Kurth S, Perdew JP, Blaha P (1999) Int J Quant Chem 75:889
121. Tao JM, Gori-Giorgi P, Perdew JP, McWeeny R (2001) Phys Rev A 63:032513
122. Caratzoulas S, Knowles PJ (2000) Mol Phys 98:1811
123. Paier J, Marsman M, Kresse G (2007) J Chem Phys 127:024103
124. Pisani C, Apra E, Causa M (1990) Int J Quant Chem 38:395
125. Gross EKU, Runge E (1986) Vielteilchentheorie. Teubner, Stuttgart
126. Ashcroft NW, Mermin ND (1976) Solid state physics. Saunders College Publishing, Orlando
127. Mahan GD (1990) Many-particle physics, 2nd edn. Plenum Press, New York
128. Cora F, Alfredsson M, Mallia G, Middlemiss DS, Mackrodt WC, Dovesi R, Orlando R (2004) The performance of hybrid density functionals in solid state chemistry. In: Kaltsoyannis N, McGrady JE (eds) Principles and applications of density in inorganic chemistry II, pp 171–232
129. Heyd J, Scuseria GE (2004) J Chem Phys 121:1187
130. Stroppa A, Kresse G (2008) New J Phys 10:063020
131. Kohn W (1995) Int J Quant Chem 56:229
132. Resta R (2006) J Chem Phys 124:104104
133. Becke AD (1996) J Chem Phys 104:1040
134. Adamo C, Barone V (1999) J Chem Phys 110:6158
135. Ernzerhof M, Scuseria GE (1999) J Chem Phys 110:5029
136. Leininger T, Stoll H, Werner HJ, Savin A (1997) Chem Phys Lett 275:151
137. Heyd J, Scuseria GE, Ernzerhof M (2003) J Chem Phys 118:8207
138. Ewald PP (1921) Ann Phys 64:253
139. Krukau AV, Vydrov OA, Izmaylov AF, Scuseria GE (2006) J Chem Phys 125:224106
140. Marsman M, Paier J, Stroppa A, Kresse G (2008) J Phys: Condens Matter 20:064201
141. Henderson TM, Paier J, Scuseria GE (2011) Phys Stat Solidi B 248:767
142. Dovesi R, Civalleri B, Orlando R, Roetti C, Saunders VR (2005) Ab initio quantum simulation in solid state chemistry. In: Lipkovitz KB, Thomas RL, Cundari TR (eds) Reviews in computational chemistry. Wiley-VCH, New York, p 1
143. Mackrodt WC, Harrison NM, Saunders VR, Allan NL, Towler MD, Apra E, Dovesi R (1993) Philos Mag A 68:653
144. Towler MD, Allan NL, Harrison NM, Saunders VR, Mackrodt WC, Apra E (1994) Phys Rev B 50:5041
145. Kudin KN, Scuseria GE, Martin RL (2002) Phys Rev Lett 89:266402
146. Frisch MJ, Trucks GW, Schlegel HB, Scuseria GE, Robb MA, Cheeseman JR, Scalmani G, Barone V, Mennucci B, Petersson GA, Nakatsuji H, Caricato M, Li X, Hratchian HP, Izmaylov AF, Bloino J, Zheng G, Sonnenberg JL, Hada M, Ehara M, Toyota K, Fukuda R, Hasegawa J, Ishida M, Nakajima T, Honda Y, Kitao O, Nakai H, Vreven T, Montgomery JA Jr, Peralta JE, Ogliaro F, Bearpark MJ, Heyd J, Brothers EN, Kudin KN, Staroverov VN, Kobayashi R, Normand J, Raghavachari K, Rendell AP, Burant JC, Iyengar SS, Tomasi J, Cossi M, Rega N, Millam NJ, Klene M, Knox JE, Cross JB, Bakken V, Adamo C, Jaramillo J, Gomperts R, Stratmann RE, Yazyev O, Austin AJ, Cammi R, Pomelli C, Ochterski JW, Martin RL, Morokuma K, Zakrzewski VG, Voth GA, Salvador P, Dannenberg JJ, Dapprich S, Daniels AD, Farkas Ö, Foresman JB, Ortiz JV, Cioslowski J, Fox DJ (2009) Gaussian 09, Gaussian 09. Gaussian Inc, Wallingford
147. VandeVondele J, Hutter J (2007) J Chem Phys 127:114105
148. Chalasinski G, Szczesniak MM (2000) Chem Rev 100:4227
149. Boys SF, Bernardi F (1970) Mol Phys 19:553
150. Blum V, Gehrke R, Hanke F, Havu P, Havu V, Ren X, Reuter K, Scheffler M (2009) Comput Phys Commun 180:2175
151. Ren X, Rinke P, Blum V, Wieferink J, Tkatchenko A, Sanfilippo A, Reuter K, Scheffler M (2012) New J Phys 14:053020
152. Tran F, Blaha P, Schwarz K, Novak P (2006) Phys Rev B 74:155108
153. Tran F, Blaha P (2011) Phys Rev B 83:235118
154. Betzinger M, Friedrich C, Blügel S (2010) Phys Rev B 81:195117
155. Friedrich C, Schindlmayr A, Blügel S (2009) Comput Phys Commun 180:347
156. Paier J, Hirschl R, Marsman M, Kresse G (2005) J Chem Phys 122:234102
157. Rostgaard C, Jacobsen KW, Thygesen KS (2010) Phys Rev B 81:085103
158. Yan J, Hummelshoj JS, Norskov JK (2013) Phys Rev B 87:075207
159. Guidon M, Hutter J, VandeVondele J (2010) J Chem Theory Comput 6:2348
160. Giannozzi P, Baroni S, Bonini N, Calandra M, Car R, Cavazzoni C, Ceresoli D, Chiarotti GL, Cococcioni M, Dabo I, Dal Corso A, de Gironcoli S, Fabris S, Fratesi G, Gebauer R, Gerstmann U, Gougoussis C, Kokalj A, Lazzeri M, Martin-Samos L, Marzari N, Mauri F, Mazzarello R, Paolini S, Pasquarello A, Paulatto L, Sbraccia C, Scandolo S, Sclauzero G, Seitsonen AP, Smogunov A, Umari P, Wentzcovitch RM (2009) J Phys Condens Matter 21:395502
161. Alkauskas A, Broqvist P, Pasquarello A (2011) Phys Stat Solidi B 248:775
162. Lee H-Y, Clark SJ, Robertson J (2012) Phys Rev B 86:075209
163. Guo Y, Clark SJ, Robertson J (2014) J Chem Phys 140:054702
164. Guo Y, Clark SJ, Robertson J (2012) J Phys: Condens Matter 24:325504
165. Anisimov VI, Zaanen J, Andersen OK (1991) Phys Rev B 44:943
166. Liechtenstein AI, Anisimov VI, Zaanen J (1995) Phys Rev B 52:R5467
167. Anisimov VI, Aryasetiawan F, Lichtenstein AI (1997) J Phys: Condens Matter 9:767
168. Dudarev SL, Botton GA, Savrasov SY, Humphreys CJ, Sutton AP (1998) Phys Rev B 57:1505
169. Mott NF (1961) Philos. Mag. 6:287
170. Mott NF (1956) Can J Phys 34:1356
171. Mott NF (1949) Proc Phys Soc Lond Sect A 62:416
172. Hubbard J (1964) Proc Phys Soc Lond Sect A 277:237; ibid 281:401
173. Herring C (1966) In: Rado GT, Suhl H (eds) Magnetism. Academic, New York
174. Solovyev IV, Dederichs PH, Anisimov VI (1994) Phys Rev B 50:16861
175. Da Silva JLF, Ganduglia-Pirovano MV, Sauer J, Bayer V, Kresse G (2007) Phys Rev B 75:045121
176. Lutfalla S, Shapovalov V, Bell AT (2011) J Chem Theory Comput 7:2218
177. Hu Z, Li B, Sun X, Metiu H (2011) J Phys Chem C 115:3065
178. Fabris S, Vicario G, Balducci G, de Gironcoli S, Baroni S (2005) J Phys Chem B 109:22860
179. Allen JP, Watson GW (2014) Phys Chem Chem Phys 16:21016
180. Deo G, Wachs IE (1994) J Catal 146:323
181. Wachs IE, Chen Y, Jehng JM, Briand LE, Tanaka T (2003) Catal Today 78:13

182. Beck B, Harth M, Hamilton NG, Carrero C, Uhlrich JJ, Trunschke A, Shaikhutdinov S, Schubert H, Freund H-J, Schlögl R, Sauer J, Schomäcker R (2012) J Catal 296:120
183. Feng T, Vohs JM (2004) J Catal 221:619
184. Ganduglia-Pirovano MV, Popa C, Sauer J, Abbott H, Uhl A, Baron M, Stacchiola D, Bondarchuk O, Shaikhutdinov S, Freund H-J (2010) J Am Chem Soc 132:2345
185. Kim T, Wachs IE (2008) J Catal 255:197
186. Wachs IE (2013) Dalton Trans 42:11762
187. Baron M, Abbott H, Bondarchuk O, Stacchiola D, Uhl A, Shaikhutdinov S, Freund H-J, Popa C, Ganduglia-Pirovano MV, Sauer J (2009) Angew Chem Int Ed 48:8006
188. Penschke C, Paier J, Sauer J (2013) J Phys Chem C 117:5274
189. Popa C, Ganduglia-Pirovano MV, Sauer J (2011) J Phys Chem C 115:7399; Erratum: (2012) ibid 116:18572
190. Kropp T, Paier J, Sauer J (2014) J Am Chem Soc 136:14616
191. Redhead PA (1962) Vacuum 12:203
192. Reuter K, Scheffler M (2001) Phys Rev B 65:035406
193. Fabris S, de Gironcoli S, Baroni S, Vicario G, Balducci G (2005) Phys Rev B 72:237102
194. Paier J, Kropp T, Penschke C, Sauer J (2013) Faraday Discuss 162:233
195. Burow AM, Wende T, Sierka M, Wlodarczyk R, Sauer J, Claes P, Jiang L, Meijer G, Lievens P, Asmis KR (2011) Phys Chem Chem Phys 13:19393
196. Jiang L, Wende T, Claes P, Bhattacharyya S, Sierka M, Meijer G, Lievens P, Sauer J, Asmis KR (2011) J Phys Chem A 115:11187
197. Kropp T, Paier J (2014) J Phys Chem C 118:23690
198. Grimme S (2006) J Comput Chem 27:1787
199. Kerber T, Sierka M, Sauer J (2008) J Comput Chem 29:2088
200. Beste A, Mullins DR, Overbury SH, Harrison RJ (2008) Surf Sci 602:162
201. Capdevila-Cortada M, García-Melchor M, López N (2015) J Catal 327:58
202. Yang C, Bebensee F, Nefedov A, Wöll C, Kropp T, Komissarov L, Penschke C, Moerer R, Paier J, Sauer J (2016) J Catal 336:116
203. Ferrizz RM, Wong GS, Egami T, Vohs JM (2001) Langmuir 17:2464
204. Vohs JM (2013) Chem Rev 113:4136
205. Rozanska X, Fortrie R, Sauer J (2007) J Phys Chem C 111:6041
206. Döbler J, Pritzsche M, Sauer J (2005) J Am Chem Soc 127:10861
207. Noodleman L (1981) J Chem Phys 74:5737
208. Hampel C, Peterson KA, Werner HJ (1992) Chem Phys Lett 190:1
209. Deegan MJO, Knowles PJ (1994) Chem Phys Lett 227:321
210. Haruta M, Kobayashi T, Sano H, Yamada N (1987) Chem Lett 16:405
211. Haruta M, Date M (2001) Appl Catal A Gen 222:427
212. Trovarelli A (2002) Catalysis by ceria and related materials. Catalytic science series, Hutchings, GJ. Imperial College Press, London
213. Fu Q, Saltsburg H, Flytzani-Stephanopoulos M (2003) Science 301:935
214. Rodriguez JA (2011) Catal Today 160:3
215. Haller GL, Resasco DE (1989) Adv Catal 36:173
216. Tauster SJ (1987) Acc Chem Res 20:389
217. Campbell CT (2012) Nat Chem 4:597
218. Vayssilov GN, Lykhach Y, Migani A, Staudt T, Petrova GP, Tsud N, Skala T, Bruix A, Illas F, Prince KC, Matolin V, Neyman KM, Libuda J (2011) Nat Mater 10:310
219. Plata JJ, Marquez AM, Fdez Sanz J (2013) J Phys Chem C 117:25497
220. Hernandez NC, Grau-Crespo R, de Leeuw NH, Sanz JF (2009) Phys Chem Chem Phys 11:5246
221. Chen Y, Hu P, Lee MH, Wang HF (2008) Surf Sci 602:1736
222. Camellone MF, Fabris S (2009) J Am Chem Soc 131:10473
223. Zhang CJ, Michaelides A, Jenkins SJ (2011) Phys Chem Chem Phys 13:22
224. Pan Y, Nilius N, Freund H-J, Paier J, Penschke C, Sauer J (2013) Phys Rev Lett 111:206101; Erratum: (2015) ibid 115:269901
225. Pyykkö P (2004) Angew Chem Int Ed 43:4412
226. Nilius N, Ganduglia-Pirovano MV, Brazdova V, Kulawik M, Sauer J, Freund HJ (2008) Phys Rev Lett 100:096802
227. Sterrer M, Risse T, Pozzoni UM, Giordano L, Heyde M, Rust H-P, Pacchioni G, Freund H-J (2007) Phys Rev Lett 98:096107
228. Kośmider K, Brázdová V, Ganduglia-Pirovano MV, Pérez R (2016) J Phys Chem C 120:927
229. Li H-Y, Wang H-F, Gong X-Q, Guo Y-L, Guo Y, Lu G, Hu P (2009) Phys Rev B 79:193401
230. Ganduglia-Pirovano MV, Da Silva JLF, Sauer J (2009) Phys Rev Lett 102:02610101
231. Branda MM, Castellani NJ, Grau-Crespo R, de Leeuw NH, Hernandez NC, Sanz JF, Neyman KM, Illas F (2009) J Chem Phys 131:094702
232. Pan Y, Cui Y, Stiehler C, Nilius N, Freund HJ (2013) J Phys Chem C 117:21879
233. Holleman AF, Wiberg E (1995) Lehrbuch der Anorganischen Chemie. Walter de Gruyter, Berlin
234. Imada M, Fujimori A, Tokura Y (1998) Rev Mod Phys 70:1039
235. Dernier PD, Marezio M (1970) Phys Rev B 2:3771
236. McWhan DB, Rice TM (1969) Phys Rev Lett 22:887
237. McWhan DB, Rice TM, Remeika JP (1969) Phys Rev Lett 23:1384
238. Held K, Keller G, Eyert V, Vollhardt D, Anisimov VI (2001) Phys Rev Lett 86:5345
239. Lantz G, Hajlaoui M, Papalazarou E, Jacques VLR, Mazzotti A, Marsi M, Lupi S, Amati M, Gregoratti L, Si L, Zhong Z, Held K (2015) Phys Rev Lett 115:236802
240. Surnev S, Ramsey MG, Netzer FP (2003) Prog Surf Sci 73:117
241. Göbke D, Romanyshyn Y, Guimond S, Sturm JM, Kuhlenbeck H, Döbler J, Reinhardt U, Ganduglia-Pirovano MV, Sauer J, Freund HJ (2009) Angew Chem Int Ed 48:3695
242. Feiten FE, Seifert J, Paier J, Kuhlenbeck H, Winter H, Sauer J, Freund H-J (2015) Phys Rev Lett 114:216101
243. Kresse G, Surnev S, Schoiswohl J, Netzer FP (2004) Surf Sci 555:118
244. Todorova TK, Ganduglia-Pirovano MV, Sauer J (2005) J Phys Chem B 109:23523
245. Feiten FE, Kuhlenbeck H, Freund H-J (2015) J Phys Chem C 119:22961
246. Czekaj I, Hermann K, Witko M (2003) Surf Sci 525:33; ibid 545:85
247. Czekaj I, Witko M, Hermann K (2003) Surf Sci 525:46
248. Window AJ, Hentz A, Sheppard DC, Parkinson GS, Woodruff DP, Unterberger W, Noakes TCQ, Bailey P, Ganduglia-Pirovano MV, Sauer J (2012) Surf Sci 606:1716
249. Window AJ, Hentz A, Sheppard DC, Parkinson GS, Niehus H, Ahlbehrendt D, Noakes TCQ, Bailey P, Woodruff DP (2011) Phys Rev Lett 107:016105
250. Wang H, Mellan TA, Grau-Crespo R, Schwingenschlögl U (2014) Chem Phys Lett 608:126
251. Wang Y, Perdew JP (1991) Phys Rev B 44:13298
252. Perdew JP, Chevary JA, Vosko SH, Jackson KA, Pederson MR, Singh DJ, Fiolhais C (1992) Phys Rev B 46:6671; Erratum: (1993) ibid 48:4978
253. Iori F, Gatti M, Rubio A (2012) Phys Rev B 85:115129

254. Cornell RM, Schwertmann U (2004) The iron oxides. Wiley-VCH, Weinheim
255. Schlögl R (2003) Angew Chem Int Ed 42:2004
256. Muan A (1958) Am J Sci 256:171
257. Ketteler G, Weiss W, Ranke W, Schlögl R (2001) Phys Chem Chem Phys 3:1114
258. Noh J, Osman OI, Aziz SG, Winget P, Bredas J-L (2014) Sci Technol Adv Mater 15:044202
259. Lennie AR, Condon NG, Leibsle FM, Murray PW, Thornton G, Vaughan DJ (1996) Phys Rev B 53:10244
260. Li X, Paier J (2016) J Phys Chem C 120:1056
261. Bucko T, Hafner J, Lebègue S, Ángyán JG (2010) J Phys Chem A 114:11814
262. Yu X, Huo C-F, Li Y-W, Wang J, Jiao H (2012) Surf Sci 606:872
263. Leonov I, Yaresko AN, Antonov VN, Korotin MA, Anisimov VI (2004) Phys Rev Lett 93:146404
264. Jeng HT, Guo GY, Huang DJ (2004) Phys Rev Lett 93:156403
265. Dementyev P, Dostert K-H, Ivars-Barceló F, O'Brien CP, Mirabella F, Schauermann S, Li X, Paier J, Sauer J, Freund H-J (2015) Angew Chem Int Ed 54:13942
266. Alecu IM, Zheng JJ, Zhao Y, Truhlar DG (2010) J Chem Theory Comput 6:2872
267. Yu X, Emmez E, Pan Q, Yang B, Pomp S, Kaden WE, Sterrer M, Shaikhutdinov S, Freund H-J, Goikoetxea I, Wlodarczyk R, Sauer J (2016) Phys Chem Chem Phys 18:3755
268. Ugliengo P, Sodupe M, Musso F, Bush IJ, Orlando R, Dovesi R (2008) Adv Mater 20:4579
269. Musso F, Sodupe M, Corno M, Ugliengo P (2009) J Phys Chem C 113:17876
270. Muscat J, Wander A, Harrison NM (2001) Chem Phys Lett 342:397
271. Oba F, Togo A, Tanaka I, Paier J, Kresse G (2008) Phys Rev B 77:245202
272. Di Valentin C, Pacchioni G, Selloni A (2006) Phys Rev Lett 97:166803
273. Kwapien K, Paier J, Sauer J, Geske M, Zavyalova U, Horn R, Schwach P, Trunschke A, Schlögl R (2014) Angew Chem Int Ed 53:8774
274. Furche F, Perdew JP (2006) J Chem Phys 124:044103
275. Heyd J, Peralta JE, Scuseria GE, Martin RL (2005) J Chem Phys 123:174101
276. Rivero P, Moreira IdPR, Scuseria GE, Illas F (2009) Phys Rev B 79:245129
277. Malrieu JP, Caballol R, Calzado CJ, de Graaf C, Guihery N (2014) Chem Rev 114:429
278. Moreira IPR, Illas F (2006) Phys Chem Chem Phys 8:1645
279. Eom T, Lim H-K, Goddard WA III, Kim H (2015) J Phys Chem C 119:556
280. Mullins DR (2015) Surf Sci Rep 70:42
281. Tuller HL, Nowick AS (1979) J Electrochem Soc 126:209
282. Panhans MA, Blumenthal RN (1993) Solid State Ionics 60:279
283. Gorte R (2010) AlChE J. 56:1126
284. Castleton CWM, Kullgren J, Hermansson K (2007) J Chem Phys 127:244704
285. Stoneham AM, Gavartin J, Shluger AL, Kimmel AV, Ramo DM, Ronnow HM, Aeppli G, Renner C (2007) J Phys: Condens Matter 19:255208
286. Deak P, Aradi B, Frauenheim T (2011) Phys Rev B 83:155207
287. Setvin M, Franchini C, Hao X, Schmid M, Janotti A, Kaltak M, Van de Walle CG, Kresse G, Diebold U (2014) Phys Rev Lett 113:086402
288. Graciani J, Marquez AM, Plata JJ, Ortega Y, Hernandez NC, Meyer A, Zicovich-Wilson CM, Sanz JF (2011) J Chem Theory Comput 7:56
289. Erba A, Mahmoud A, Belmonte D, Dovesi R (2014) J Chem Phys 140:124703
290. Knuth F, Carbogno C, Atalla V, Blum V, Scheffler M (2015) Comput Phys Commun 190:33
291. Chevrier VL, Ong SP, Armiento R, Chan MKY, Ceder G (2010) Phys Rev B 82:075122
292. Kübler J (1980) J Magn Magn Mater 20:277
293. Hobbs D, Hafner J, Spisak D (2003) Phys Rev B 68:014407
294. Schimka L, Gaudoin R, Klimes J, Marsman M, Kresse G (2013) Phys Rev B 87:214102
295. Feibelman PJ, Hammer B, Norskov JK, Wagner F, Scheffler M, Stumpf R, Watwe R, Dumesic J (2001) J Phys Chem B 105:4018
296. Schimka L, Harl J, Stroppa A, Grüneis A, Marsman M, Mittendorfer F, Kresse G (2010) Nat Mater 9:741
297. Kresse G, Gil A, Sautet P (2003) Phys Rev B 68:073401
298. Olsen RA, Philipsen PHT, Baerends EJ (2003) J Chem Phys 119:4522
299. Harl J, Kresse G (2009) Phys Rev Lett 103:056401
300. Lazic P, Alaei M, Atodiresei N, Caciuc V, Brako R, Blügel S (2010) Phys Rev B 81:045401
301. Huang C, Pavone M, Carter EA (2011) J Chem Phys 134:154110
302. Sharifzadeh S, Huang P, Carter E (2008) J Phys Chem C 112:4649
303. Scuseria GE, Jimenez-Hoyos CA, Henderson TM, Samanta K, Ellis JK (2011) J Chem Phys 135:124108
304. Tsuchimochi T, Scuseria GE (2011) J Chem Phys 134:064101
305. Held K, Nekrasov IA, Keller G, Eyert V, Blümer N, McMahan AK, Scalettar RT, Pruschke T, Anisimov VI, Vollhardt D (2006) Phys Stat Solidi B 243:2599
306. Eyert V (2011) Phys Rev Lett 107:016401
307. Grau-Crespo R, Wang H, Schwingenschlögl U (2012) Phys Rev B 86:081101
308. Zheng H, Wagner LK (2015) Phys Rev Lett 114:176401
309. Schrön A, Rödl C, Bechstedt F (2010) Phys Rev B 82:165109
310. Paier J, Marsman M, Kresse G (2008) Phys Rev B 78:121201
311. Seo D-H, Urban A, Ceder G (2015) Phys Rev B 92:115118
312. Gerosa M, Bottani CE, Caramella L, Onida G, Di Valentin C, Pacchioni G (2015) Phys Rev B 91:155201
313. Gygi F, Baldereschi A (1986) Phys Rev B 34:4405
314. Onida G, Reining L, Rubio A (2002) Rev Mod Phys 74:601
315. Pacchioni G (2014) Catal Lett 145:80
316. Menendez-Proupin E, Palacios P, Wahnon P, Conesa JC (2014) Phys Rev B 90:045207
317. Hutchinson M, Widom M (2012) Comput Phys Commun 183:1422
318. Orlando R, Delle Piane M, Bush IJ, Ugliengo P, Ferrabone M, Dovesi R (2012) J Comput Chem 33:2276
319. Guidon M, Schiffmann F, Hutter J, VandeVondele J (2008) J Chem Phys 128:214104
320. Scuseria GE, Henderson TM, Sorensen DC (2008) J Chem Phys 129:231101
321. Scuseria GE, Henderson TM, Bulik IW (2013) J Chem Phys 139:104113
322. Kaltak M, Klimes J, Kresse G (2014) Phys Rev B 90:054115
323. Del Ben M, Schuett O, Wentz T, Messmer P, Hutter J, VandeVondele J (2015) Comput Phys Commun 187:120
324. Bechstedt F, Fuchs F, Kresse G (2009) Phys Stat Solidi B 246:1877
325. Fuchs F, Furthmüller J, Bechstedt F, Shishkin M, Kresse G (2007) Phys Rev B 76:115109
326. Wesolowski TA, Warshel A (1993) J Phys Chem 97:8050
327. Ramo DM, Gavartin JL, Shluger AL, Bersuker G (2007) Phys Rev B 75:205336

328. Giordano L, Sushko PV, Pacchioni G, Shluger AL (2007) Phys Rev B 75:024109
329. Müller C, Hermansson K (2009) Surf Sci 603:3329
330. Burow AM, Sierka M, Döbler J, Sauer J (2009) J Chem Phys 130:174710
331. Boese AD, Sauer J (2013) Phys Chem Chem Phys 15:16481
332. Jacob CR, Neugebauer J (2014) WIREs Comput Mol Sci 4:325
333. Libisch F, Huang C, Carter EA (2014) Acc Chem Res 47:2768
334. Goodpaster JD, Barnes TA, Manby FR, Miller TF III (2012) J Chem Phys 137:224113
335. Manby FR, Stella M, Goodpaster JD, Miller TF III (2012) J Chem Theory Comput 8:2564
336. Goodpaster JD, Barnes TA, Manby FR, Miller TF III (2014) J Chem Phys 140:18A507
337. Yu K, Libisch F, Carter EA (2015) J Chem Phys 143:102806
338. Becke AD (2014) J Chem Phys 140:18A301